nature aging

Article

https://doi.org/10.1038/s43587-026-01132-z

DREAM repressive activity links somatic mutation, lifespan and disease

Received: 5 October 2025

Accepted: 23 April 2026

Published online: 02 June 2026

Check for updates

Zane Koch[1], Shuvro P. Nandi[2,3], Kate Licon[3], Arturo Bujarrabal-Dueso[4,5], David H. Meyer[4,5], Safa Saeed[2], Piruntha Perampalam[6], Frederick A. Dick[6], Björn Schumacher[4,5], Ludmil B. Alexandrov[1,2,3] & Trey Ideker[1,2,3]

The DREAM complex has emerged as a central repressor of DNA repair, raising questions as to whether such repression exerts long-term effects on human health. Here we establish that DREAM-associated activity significantly impacts lifetime somatic mutation burden, and that such effects are linked to altered lifespan and age-related disease pathology. First, joint profiling of DREAM-associated activity (quantified from the expression of genes transcriptionally repressed by DREAM) and somatic mutations across a single-cell atlas of 21 mouse tissues shows that cellular niches with lower DREAM-associated activity have decreased mutation rates. Second, DREAM-associated activity predicts the varied lifespans observed across 92 mammals, with low activity marking longer-lived species. Third, reduced DREAM-associated activity in individuals with Alzheimer's disease predicts late disease onset and decreased risk for severe neuropathology. Finally, DREAM knockout in mice protects against mutation accumulation, reducing single-base substitutions by 4.2% and insertion/deletions by 19.6% in the brain. These findings position DREAM as a key regulator of aging.

To protect against the constant barrage of DNA lesions arising from endogenous cellular processes and exogenous damaging agents, organisms have evolved an extensive network of DNA repair mechanisms[1]. These mechanisms are especially effective in long-lived species, which exhibit increased resistance to cellular stresses[2,3], decreased somatic mutation rates[4,5], and more efficient DNA repair[6]. Elevated DNA repair activity is also present in reproductive (germline) tissues, yielding mutation rates that are up to 100-fold lower than in the soma[7–9]. Genomic studies in centenarians have found strong enrichments for specific genetic variants associated with DNA repair pathways[10–12]; conversely, genomic instability is a common feature of nearly all progeroid diseases[13,14] and has been reported to engender numerous phenotypes of old age including neuroinflammation[15], type 2 diabetes[16], kidney dysfunction[17,18] and Alzheimer's disease (AD)[19–22]. This prioritization of DNA repair in long-lived species, reproductive tissues, and centenarians underscores the importance of genomic integrity to longevity and raises questions about how such differences in DNA repair arise.

Recently, a protein complex known as DREAM has been shown to transcriptionally repress DNA repair pathways in somatic cells, where these pathways are not necessary for reproductive success[23]. The DREAM complex (named for its subcomponents, Dp, Rb-like-1, E2f And MuvB) was originally characterized as a repressor of the cell cycle[24]. It forms as cells enter quiescence (G0 phase), when MuvB is phosphorylated by the dual-specificity tyrosine-regulated kinase 1A

[1]Program in Bioinformatics and Systems Biology, University of California, San Diego, La Jolla, CA, USA. [2]Department of Bioengineering, University of California, San Diego, La Jolla, CA, USA. [3]Department of Medicine, University of California, San Diego, La Jolla, CA, USA. [4]Institute for Genome Stability in Aging and Disease, Medical Faculty, University and University Hospital of Cologne, Cologne, Germany. [5]Cologne Excellence Cluster for Cellular Stress Responses in Aging-Associated Diseases (CECAD), Center for Molecular Medicine Cologne (CMMC), University of Cologne, Cologne, Germany. [6]Department of Pathology and Laboratory Medicine, Verspeeten Family Cancer Centre, Children's Health Research Institute, Western University, London, Ontario, Canada. e-mail: tideker@health.ucsd.edu

https://doi.org/10.1038/s43587-026-01132-z

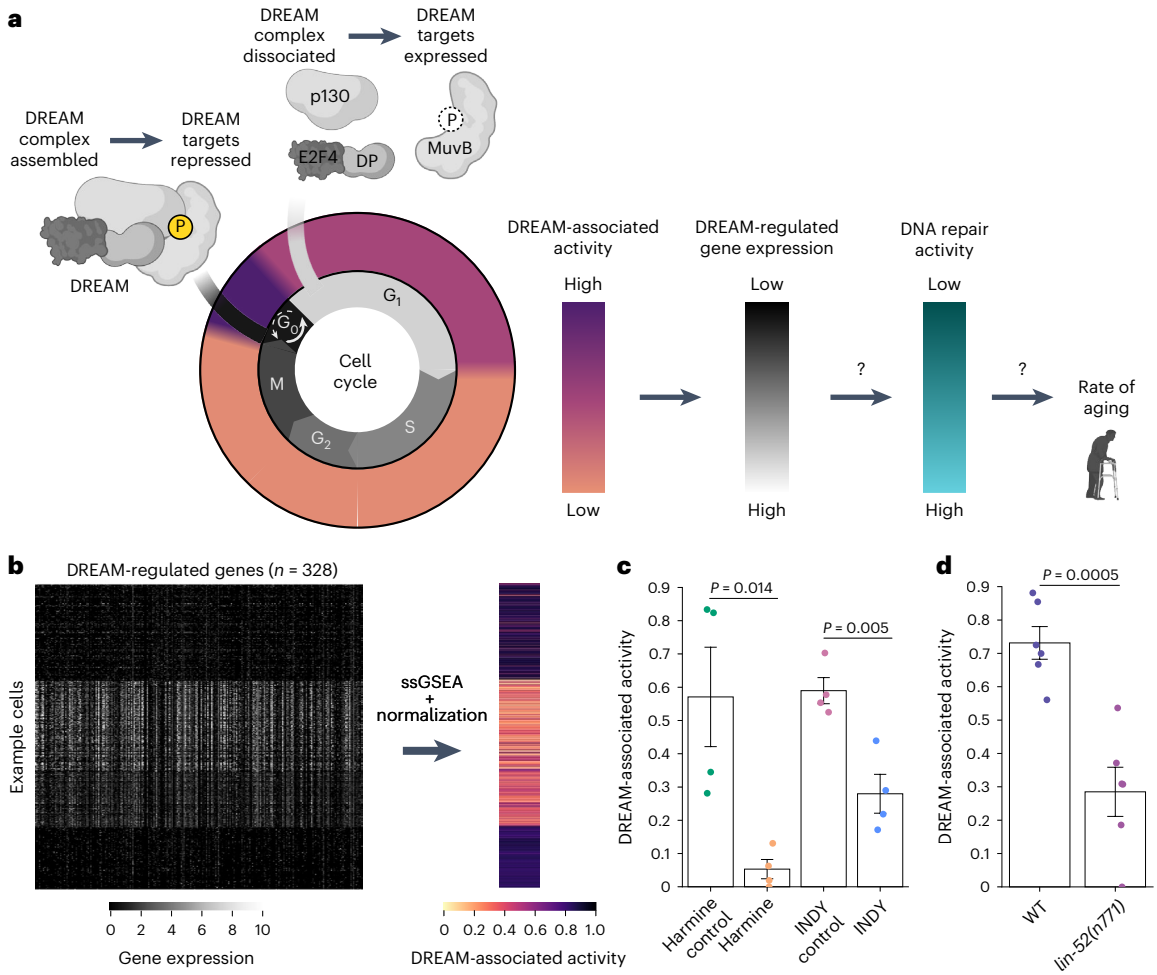

Fig. 1 | Transcriptional measurement of DREAM complex activity. **a**, The DREAM transcriptional repressor complex is formed in G0 following the phosphorylation of MuvB by DYRK1A. Upon reentry to the cell cycle, the DREAM complex dissociates and DREAM-target genes can be expressed. Here we explore the relationship between DREAM activity and somatic mutation, as well as between DREAM activity and rate of aging. Panel **a** created in BioRender; Koch, Z. https://biorender.com/8abahux (2026). **b**, Calculation of DREAM-associated activity from target gene expression. Single-sample gene set enrichment analysis (ssGSEA) is used to summarize the messenger RNA expression values of all detected DREAM complex target genes (columns, 328 DREAM-regulated genes) in each cell (rows). This ssGSEA score is then normalized and corrected for sequencing depth to produce a per-cell DREAM-associated activity score (Methods). **c**, U2OS cells are exposed to a DREAM complex inhibitor (harmine and INDY) versus control treatment (harmine control, INDY control). mRNA expression profiles are measured, from which we compute DREAM-associated activity. Bar heights indicate mean DREAM-associated activity across samples ($n = 4$ biological replicates), error bars denote 95% confidence intervals (CIs) and P values indicate the result of two-sided t-tests. **d**, Similar to **c**, but showing DREAM complex activity in wild type (WT) versus *lin-52*(*n771*) mutant *Caenorhabditis elegans*.

(DYRK1A)[25], leading to DREAM formation and the repression of numerous target genes[26,27]. To later exit quiescence, the components of the DREAM complex are prompted to dissociate by the phosphorylation of p130 (encoded by *RBL2*) by cyclin-dependent kinases[24,28], lifting repression of DREAM targets[26]. Following these cell-cycle studies, the direct targets of the DREAM complex have been shown to include many genes functioning in DNA damage response (DDR)[23,29]. Disruption of DREAM in nematode worms, progeroid mice or human cells produces resistance to DNA damaging agents[23].

Collectively, these recent results have extended the role of DREAM from repression of cell cycle to repression of DDR and its associated functions. Here we seek to determine if the DREAM complex not only governs the cell cycle and DNA repair but also hallmarks of aging and longevity (Fig. 1a). We find that, at the cellular level, DREAM-associated activity tracks with somatic mutation rate; across species, DREAM-associated activity inversely correlates with maximum lifespan; in humans, diminished DREAM-associated activity predicts later and less severe AD pathology; and in mice, induced DREAM deficiency slows the rate of somatic mutation.

Results

Transcriptional readout of DREAM repressor activity

We selected genes with regulatory regions previously shown to be bound by multiple components of the DREAM complex through protein-DNA interactions[23,24] ($n = 328$ genes). The expression of these DREAM-target genes was used to score DREAM complex-associated activity (Methods), signed such that low expression corresponds to high DREAM-associated activity (Fig. 1a,b).

The utility of this DREAM-associated activity score was underscored by several observations. First, in human tissues this score was tightly associated with the protein abundance and modification status of the DREAM subunits MuvB and p107/p130, whose phosphorylation status controls DREAM assembly[28] (Pearson $r = 0.70$, $P = 6.8 \times 10^{-15}$, $n = 160$ human individuals) (Extended Data Fig. 1a,b and Methods). Second, the score successfully distinguished cells treated with DREAM complex inhibitors[23], harmine or INDY, from those of control cells (Fig. 1c). Third, gene expression analysis of nematode worms with a mutation in *lin-52*, which causes defects in DREAM complex assembly, yielded an activity score that was markedly lower than that of wild-type

(WT) worms[23] (Fig. 1d). Fourth, increased DREAM-associated activity was associated with lower expression of the proliferative markers *MKI67*, *PCNA* and *FOXM1* across cell types (Extended Data Fig. 1c, e, g) and tissues (Extended Data Fig. 1d, f, h), as would be expected given the DREAM complex's role as a negative regulator of the cell cycle[24,26]. Notably, the expression of DNA repair genes also annotated as DREAM targets ($n = 67$), was on average 3.8-fold higher in the 20% of cells with the lowest DREAM-associated activity (Extended Data Fig. 1i,j). Collectively, these results suggested that the DREAM-associated activity score is an informative and specific metric for quantifying the repressive activity of the DREAM complex, which we also found is robust to confounding from related regulatory programs and to alternate definitions of DREAM-target genes (Supplementary Note 1 and Extended Data Fig. 2).

Somatic mutation rate tracks DREAM-associated activity in single cells

We used this DREAM-associated activity measure to study the connection between DREAM and somatic mutation. For this purpose, we analyzed the Tabula Muris Senis (TMS) dataset (Supplementary Table 1)[30], which includes full-length RNA sequencing[31] of single cells collected from 21 organs in 18 C57BL/6JN mice at young (3 months), middle (18 months), or old (24 months) age. DREAM-associated activity was scored in the single-cell RNA sequencing (scRNA-seq) data of each of 110,824 cells, revealing a broad range of values that varied substantially across organs and individual mice, and decreased with age (Extended Data Fig. 3a–c).

Somatic mutations were called from the same scRNA-seq data, leveraging a previous analysis[30] (Methods). Here we observed that the overall burden of somatic mutations increased with age in nearly every tissue (Fig. 2a), corresponding to rates of mutation ranging from a low of 0.0025 mutations per kilboase per month (tongue) to a high of 0.0045 (kidney).

Notably, in the vast majority of tissues, cells with high DREAM-associated activity had significantly greater mutation burdens than those exhibiting low activity (Fig. 2b–e and Extended Data Fig. 3d,e). For example, kidney cells in the top quintile of DREAM-associated activity showed a 2.4-fold increase in somatic mutations per kilobase compared to cells in the bottom quintile ($P = 3.3 \times 10^{-49}$, $n = 180$ cells per quintile, two-sided Mann–Whitney *U*-test). This positive association between DREAM-associated activity and mutation burden was observed not only at the tissue level but also within individual cell types within a tissue. For instance, liver hepatocytes with greater DREAM-associated activity had significantly greater mutation burdens at each age (Fig. 2f), and this was the case for the majority of cell types (Fig. 2g) and tissues (Fig. 2h) even when correcting for cell proliferation rate (Extended Data Fig. 3f,g). In contrast to DREAM-target genes, the expression levels of randomly chosen gene sets were not significantly associated with mutation burden (cell types, $P = 2.6 \times 10^{-32}$; tissue types, $P = 4.86 \times 10^{-14}$) (Fig. 2g,h and Methods).

DREAM-associated activity predicts lifespan and mutation rate across 92 species

To relate these results to lifespan, we scored DREAM-associated activity in the transcriptomes of 92 mammalian species, broadly spanning six taxonomic orders[32] (approximately three individuals × three tissues per species, $n = 803$ samples; Methods and Fig. 3a). Comparing DREAM-associated activity scores to the maximum lifespan) of each species, we observed a strong inverse relationship (Fig. 3b). Negative associations were observed across all tissues profiled (Fig. 3c) and became even stronger after controlling for the adult weight of each species (Spearman ρ, liver −0.59, $P = 6.23 \times 10^{-24}$; brain −0.46, $P = 1.26 \times 10^{-13}$; and kidney −0.30, $P = 6.23 \times 10^{-06}$; Fig. 3d and Extended Data Fig. 4a,b). Furthermore, DREAM-associated activity levels tended to be coordinated across all tissues within a species (Fig. 3e).

Comparing the DREAM-associated activity of liver, brain, and kidney tissues to previous measurements of species-specific somatic mutation rates[4] ($n = 11$ species), we found that DREAM complex activity in the liver and brain was positively correlated with somatic mutation rate across species (liver, $\rho = 0.61$, $P = 6.0 \times 10^{-4}$; brain, $\rho = 0.49$, $P = 0.008$; and kidney, $\rho = -0.31$, $P = 0.12$) (Fig. 3f, Extended Data Fig. 4c–g and Methods). Further linking DREAM complex activity to species-specific DNA repair capacity, we observed that fibroblasts from species with lower DREAM complex activity exhibited greater resistance to various stress-inducing agents including the mitochondrial respiration inhibitor rotenone; the oxidative damage inducing agents cadmium and paraquat; the alkylating agent methyl methanesulfonate (MMS); UV radiation; and heat ($n = 37$ cell lines from six species[2]) (Extended Data Fig. 5a–h and Methods). These results indicated that the amount of DREAM complex activity within a species is associated with the lifespan of that species, as well as its somatic mutation rate and resistance to DNA damage.

Low DREAM-associated activity promotes resilience to a high-fat diet

A high-fat diet (HFD) has been shown to shorten lifespan and induce genomic instability in multiple species[33–35], associated with an increased burden of oxidative damage and rate of somatic mutation[36]. Using a large cohort of mice from 50 distinct inbred strains[37] ($n = 882$ mice; Extended Data Fig. 6a), half fed an HFD (60% calories from fat) and half fed a regular chow diet (CD; 6% calories from fat), we investigated whether strains with lower DREAM-associated activity were protected from the harms of HFD leading to extended survival.

Fig. 2 | Association between DREAM-associated activity and single-cell somatic mutation rate. a, Box plots of the distribution of somatic mutation burden across the cells of each tissue at each age ($n = 110{,}824$ cells, $n = 18$ mice). Mutation burden is expressed as the mutation count per callable kilobase (Methods). Two-sided *P* values calculated by modeling Spearman ρ as a Student's *t*-test distribution; $^{***}P < 5.0 \times 10^{-19}$, NS, $P \geq 0.01$. BAT, brown adipose tissue; GAT, gonadal adipose tissue; MAT, mesenteric adipose tissue; SAT, subcutaneous adipose tissue. Boxes show interquartile range (IQR) with median line; whiskers extend to 1.5 × IQR. **b**, The somatic mutation burden per kb in cells from 18-month-old mice ($n = 34{,}027$ cells, $n = 4$ mice) stratified by DREAM complex activity (highest versus lowest 20% of DREAM complex activities within each tissue). Points denote means and error bars 95% CIs. $^{*}P < 0.0023$ (Bonferroni-corrected), NS, $P \geq 0.0023$, based on a two-sided Mann–Whitney *U*-test. **c**, Uniform manifold approximation and projection (UMAP) of all cells of all age mice from the first 12 tissue types in **b** (from the left, $n = 42{,}508$ cells, $n = 18$ mice), colored by cell type and labeled with tissue of origin. **d**, As in **c** but coloring cells by DREAM-associated activity. Cells with the 50% lowest and 50% highest DREAM activities for age and tissue type are colored orange and purple, respectively. **e**, As in **d** but coloring cells by somatic mutation burden per kb. Cells with the 50% lowest and 50% highest somatic mutation burdens for their age and tissue type are colored light green and blue, respectively. **f**, Violin plot of the somatic mutation burden in hepatocyte cells ($n = 1{,}162$ cells, $n = 18$ mice) stratified by age and DREAM complex activity. $^{***}P < 5.0 \times 10^{-200}$; significant Spearman correlation between DREAM complex activity and mutation burden within an age group. Spearman ρ, 3 months ρ = 0.16; 18 months ρ = 0.30; and 24 months ρ = 0.21. Vertical bars inside each violin represent the interquartile range. Two-sided *P* value calculated by modeling Spearman ρ as a Student's *t*-test distribution. **g**, Kernel density plot depicting the distribution of Spearman ρ computed in each cell type ($n = 116$ cell types, $n = 34{,}027$ cells from 18-month-old mice, $n = 4$ mice) between somatic mutation burden and gene set activity scores (ssGSEA; Methods). Purple, DREAM-regulated gene set ($n = 248$ genes). Gray, 500 random gene sets ($n = 248$ random genes per set). $^{***}P < 4.86 \times 10^{-14}$; significant difference in Spearman correlation values between groups based on a two-sided Mann–Whitney *U*-test. **h**, Similar to **g**, but comparing somatic mutation burden and gene expression within tissue types ($n = 21$ tissue types, $n = 34{,}027$ cells from 18-month-old mice, $n = 4$ mice; Methods).

https://doi.org/10.1038/s43587-026-01132-z

For each strain and diet, 70% of mice (n = 612 mice) were followed to measure lifespan, while the remaining 30% were euthanized and transcriptionally profiled to score DREAM-associated activity (n = 270 mouse livers). Lifespan and DREAM-associated activity varied greatly across strains (median lifespan= 704 ± 147 days; mean ± s.d.; Methods), with HFD mice having markedly shorter lifespans than CD mice (median survival, HFD = 640 days, CD = 730 days) (Extended Data Fig. 6b–f). Notably, strains with lower DREAM-associated activity had extended survival on the HFD compared to those with higher DREAM-associated activity (median survival, lowest 20% DREAM-associated activity = 678 days, highest 20% DREAM-associated activity = 578 days; Fig. 4a,b). Controlling for sequencing depth and physiological factors, including weight, weight gain on diet and blood lipid levels (Extended Data Fig. 6g and Methods), a 1 × s.d. increase in DREAM-associated activity corresponded to a 36% increase in risk of death for HFD mice (hazard ratio 1.36, $P = 9.0 \times 10^{-4}$) (Fig. 4b). When fed the chow diet, there was no

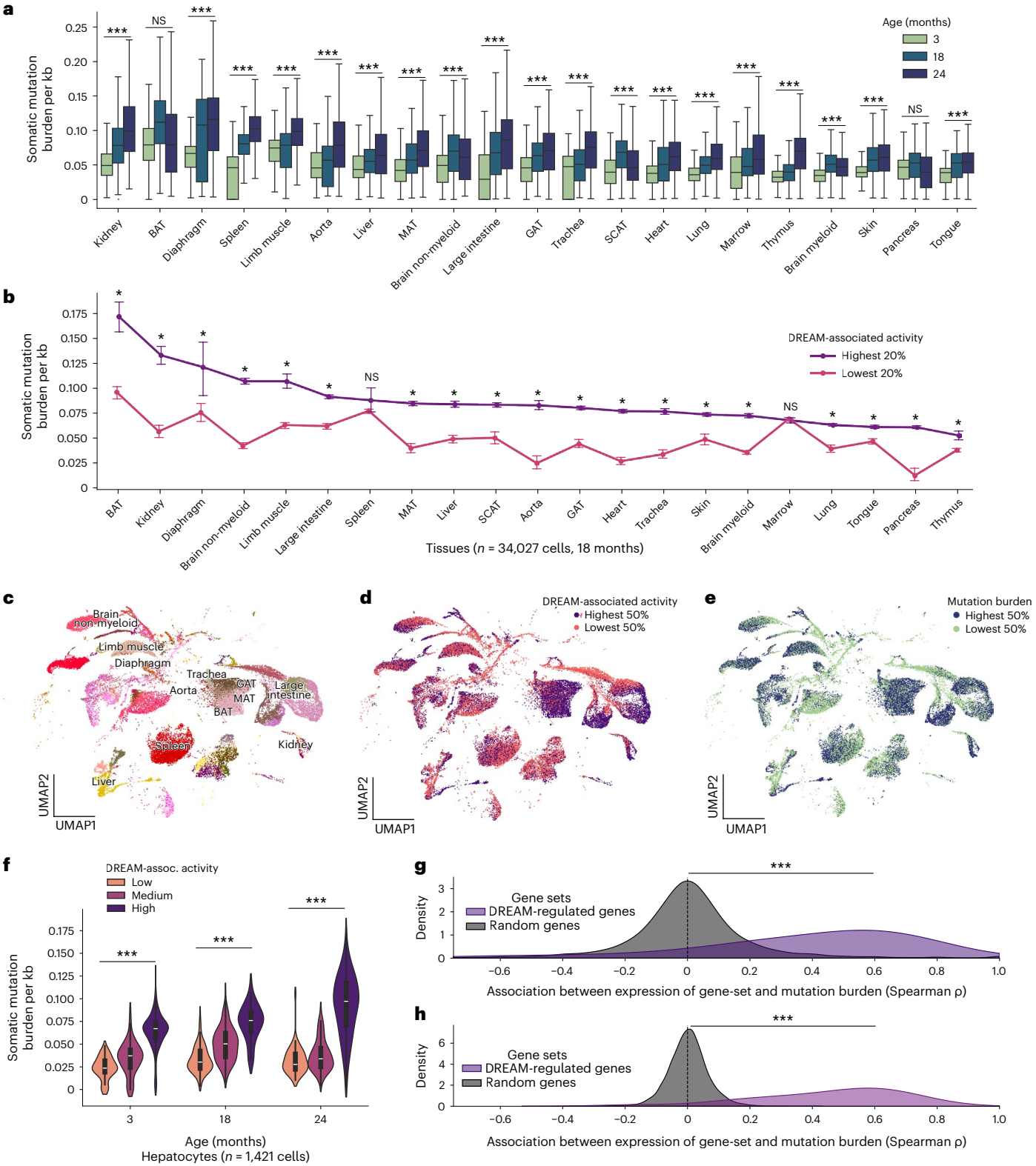

https://doi.org/10.1038/s43587-026-01132-z

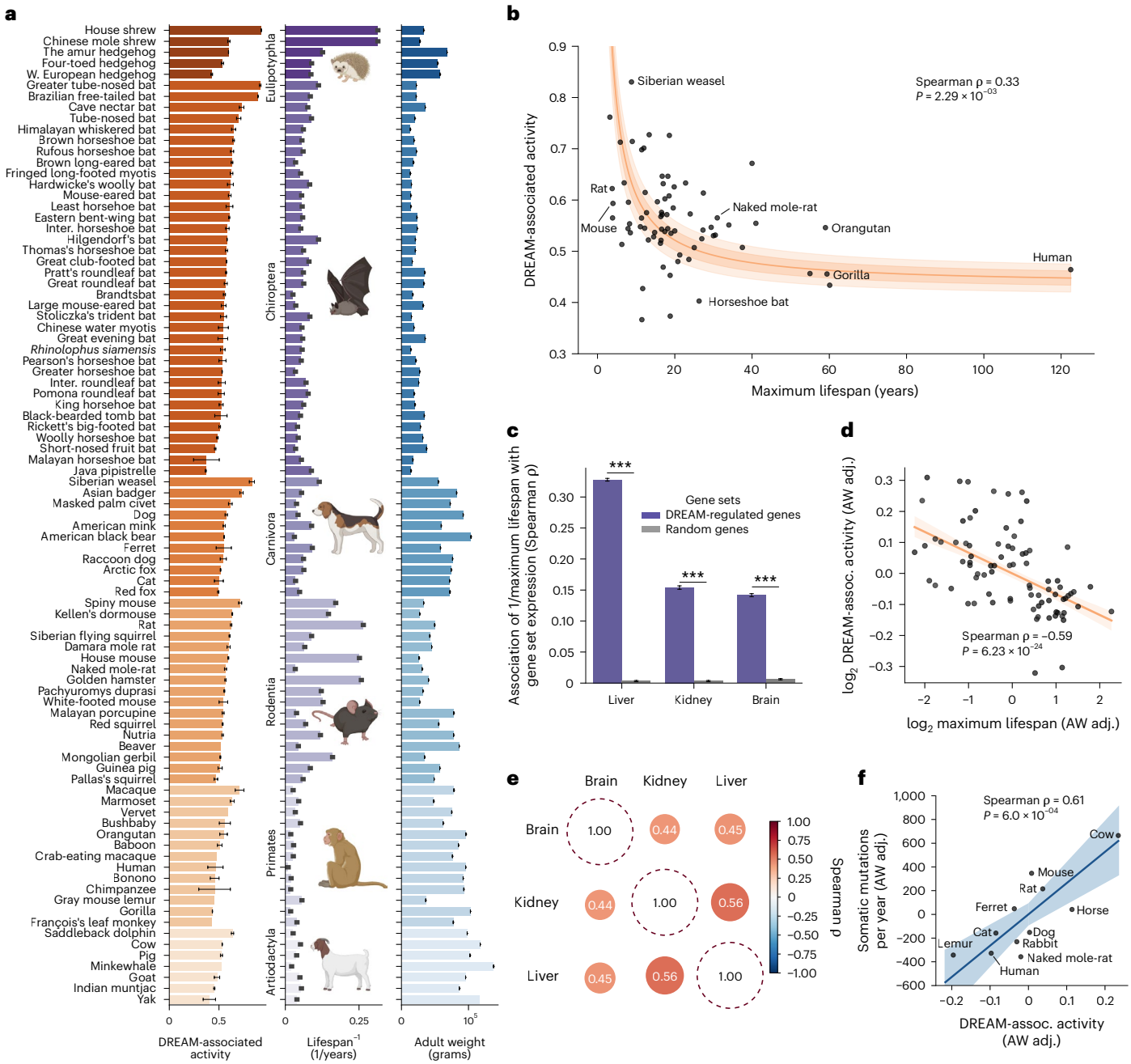

Fig. 3 | Inverse relation between DREAM-associated activity and lifespan across species. a, Barplots indicating the DREAM-associated activity across tissues (liver, kidney and brain), 1/maximum lifespan and $\log_{10}$-transformed adult weight in grams for each species ($n = 92$ species and 803 samples). Within each taxonomic order, species are sorted by decreasing average DREAM complex activity. Data are mean and s.e.m. **b**, Scatter-plot of maximum lifespan versus DREAM-associated activity measured in the liver ($n = 92$ species and 241 samples, Methods). Points indicate the mean value of each species, while the orange curve shows reduced major axis regression line fit to the actual values of all samples. The inner shaded area indicates 1 × s.d. from the regression line and the outer the 95% CI. Two-sided *P* value calculated by modeling Spearman ρ as a Student's *t*-test distribution. **c**, Barplots indicating the mean ± 99% CI of the Spearman correlation between 1/lifespan and average DREAM-associated activity of each species, in each tissue, iteratively leaving one species out ($n = 92$ species). ***$P < 8.23 \times 10^{-24}$; two-sided Mann–Whitney *U*-test. **d**, Scatter-plot and reduced major axis regression depicting the average adult weight (AW)-adjusted DREAM-associated activity and lifespan of the species in **a** ($n = 92$ species and 241 liver samples, Methods). Both axes are shown on a logarithmic scale. Shading denotes the 95% CI of the fitted regression. *P* value calculated by modeling Spearman ρ as a Student's *t*-test distribution. **e**, Heatmap of the Spearman correlation coefficients comparing DREAM-associated activity scores between each pair of tissues, across the species and samples in **a**. All pairwise correlations are significant ($P < 0.0005$), based on modeling Spearman ρ as a Student's *t*-test distribution. Two-sided *P* values were calculated. **f**, Scatter-plot and reduced major axis regression depicting the average adult weight-adjusted DREAM-associated activity and somatic mutation rate (in the liver and colon, respectively) across species ($n = 11$ species, Methods). Shading denotes the 95% CI of the fitted regression. *P* value calculated by modeling Spearman ρ as a Student's *t*-test distribution.

significant difference in survival linked to DREAM-associated activity (hazard ratio 0.93, $P = 0.27$) (Fig. 4b and Extended Data Fig. 6h).

We considered whether the association between DREAM-associated activity and lifespan in the HFD mice could be confounded by effects of the HFD itself, whereby the diet increased DREAM-associated activity while decreasing lifespan; however, this interpretation was contradicted by the observation that the DREAM complex activity of a strain when fed the chow diet was indicative of the survival of mice

https://doi.org/10.1038/s43587-026-01132-z

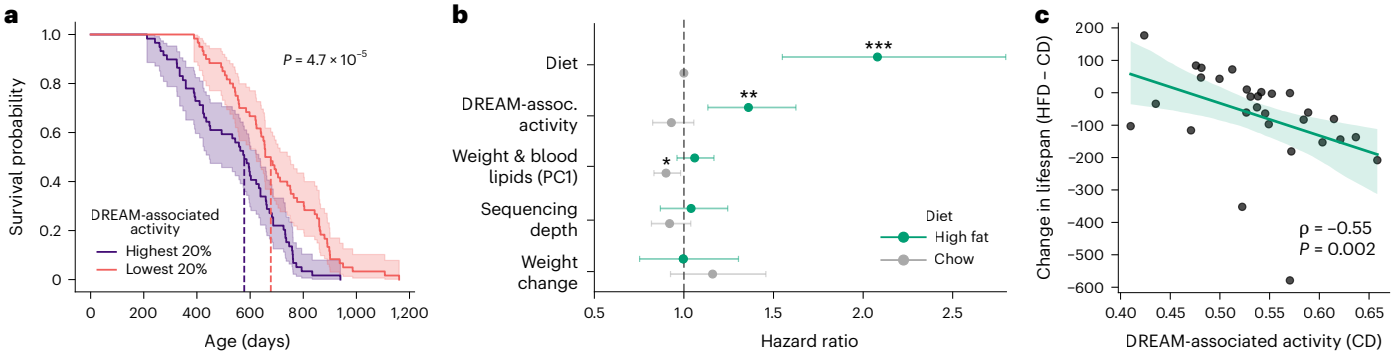

Fig. 4 | Lifespan of mice with low versus high DREAM-associated activity. **a**, Kaplan–Meier survival curve of HFD-fed mice belonging to strains with the highest versus lowest 20% of DREAM complex activities (purple versus pink, $n = 119$ mice, $n = 14$ strains). The dark line and shaded area indicate the proportion of mice surviving to a particular age and the 95% CI of this survival estimate, respectively. Dashed lines indicate the median survival of each group. *P* value calculated using a two-sided log-rank test. **b**, Dot-and-whisker plot indicating the association of each variable on the *y* axis with mouse survival, for mice fed the HFD (green, $n = 299$ mice) or CD (gray, $n = 313$ mice). Dots and whiskers indicate the hazard ratio and 95% CIs from a Cox proportional hazard model (Methods). *P* values are from a two-sided Wald test; $^{***}P < 5.0 \times 10^{-6}$, $^{**}P < 0.005$, $^{*}P < 0.05$. **c**, Scatter-plot of mean DREAM-associated activity of each mouse strain on the CD (*x* axis), compared to the change in survival when members of that strain are placed on the HFD. $n = 29$ strains profiled on both diets; $n = 10$ mice per diet per strain on average. *P* value calculated by modeling Spearman ρ as a Student's *t*-test distribution. Shading denotes the 95% CI of the fitted regression.

of the same strain when fed the HFD (Spearman $\rho = -0.55$, $P = 0.002$; Fig. 4c); that is, higher chow diet DREAM-associated activity predicted shortened survival when challenged by the HFD. Collectively, these findings suggested that inherent differences in DREAM-associated activity determine resilience to HFD-induced stress, with lower DREAM-associated activity conferring a survival advantage under metabolic challenge.

DREAM-associated activity is linked to neuropathy and Alzheimer's disease

We next moved from mice to human samples to test the relevance of our results to diseases associated with human aging. For this purpose, we applied the SComatic[38] method to identify somatic single-nucleotide substitution mutations in 803,122 single cells profiled using single-cell RNA sequencing by the Tabula Sapiens[39] and Seattle Alzheimer's Disease Brain Cell Atlas (SEA-AD[40]) consortia (Fig. 5a and Methods). Cells had been drawn from 11 tissues of 90 human individuals, including 80 with AD and 10 without disease, with donors ranging from 33 to 102 years of age (85.2 ± 13.5 years, mean ± s.d.). Somatic mutations accumulated in tissues at varying rates: from approximately 5 per cell per year in bladder and lung cells, to 10 in brain cells (Fig. 5b), and 22 in fat cells (Fig. 5c and Extended Data Fig. 7a–f). Notably, we observed that human cells with the highest DREAM-associated activity in each tissue obtained somatic mutations at substantially greater rates than the cells with the lowest DREAM-associated activity (Fig. 5d), replicating the results we found in mice (Fig. 2).

Neuropathological data had been collected at the time of death for individuals with AD ($n = 80$). We found that increased Braak score (a measure of tau pathology), AD neuropathologic change (ADNC) score (a composite measure of amyloid plaques, neurofibrillary tangles and neuritic plaques), and somatic mutation burden were all associated with greater DREAM-associated activity (Fig. 5e and Methods). In an independent dataset of postmortem brains from individuals with neurodegeneration (Religious Orders Study/Memory and Aging Project (ROSMAP)[41], $n = 1{,}101$ individuals), elevated DREAM-associated activity was linked to earlier AD diagnosis (Fig. 5f). Controlling for covariates, a 1 × s.d. increase in DREAM-associated activity corresponded to a 21% increase in the risk of AD at a given age (HR = 1.21, $P = 0.01$; Fig. 5g). Unlike DREAM-target genes, the expression of randomly selected sets of genes did not exhibit a significant association with AD diagnosis risk (mean HR = 1.0; Extended Data Fig. 7h,i). As an alternative explanation, we also considered that cells with the highest DREAM-associated activity might be resistant to neuronal loss, such that the longer an individual had AD before death, the higher their DREAM-associated activity would become; however, DREAM-associated activity was not correlated with the duration of AD before death (Extended Data Fig. 7j), inconsistent with such survivor bias.

These results indicated that DREAM activity is associated with human dysfunction at multiple biological scales: somatic mutations at the genomic level, neuropathology at the cellular level and AD at the organismal level.

DREAM loss of function reduces mutation accumulation in vivo

Finally, we tested whether DREAM activity is a causal driver of mutation accumulation in vivo by preventing DREAM complex assembly in mice and quantifying lifetime somatic mutation burden. We analyzed formalin-fixed paraffin-embedded (FFPE) brains from DREAM loss-of-function (LoF)[42] mice ($n = 4$, $p107^{D/D}p130^{-/-}$) and littermate controls ($n = 5$; $p107^{D/D}p130^{fl/fl}$; where $p107^{D/D}$ denotes a constitutive *Rbl1* missense allele, and *p130* is also known as *Rbl2*) (Fig. 6a). At 8 weeks of age, both groups had received tamoxifen, preventing DREAM assembly only in the DREAM LoF mice, whereas littermate controls retained intact DREAM function[42]. Brain tissue was collected after natural death and profiled for somatic mutations using single-molecule duplex sequencing (Methods).

Controlling for covariates (Extended Data Fig. 8a–f), we found that DREAM LoF mice exhibited a 4.2% reduction in single-base substitution (SBS) mutations per cell compared to controls (Fig. 6b and Methods). Across samples, the operative mutational signatures (distinctive mutation patterns that reflect the underlying source of somatic mutations[43]) were SBS1, SBS5 and SBS30, as well as the characteristic mutational signature of formalin fixation[44]. SBS1 reflects spontaneous deamination of 5-methylcytosine and SBS5 is a ubiquitous clock-like process of uncertain origin (both are classical age-related signatures), whereas SBS30 is linked to base-excision repair defects[45]. The proportion of mutations attributed to each mutational signature was not significantly different between groups, suggesting that loss of DREAM reduces overall mutagenesis rather than selectively altering a single repair pathway (Fig. 6c,d).

We observed that DREAM loss-of-function also conferred protection from insertion and deletion (ID, also known as indel) mutations. Relative to controls, DREAM LoF mice had 19.6% fewer ID mutations

https://doi.org/10.1038/s43587-026-01132-z

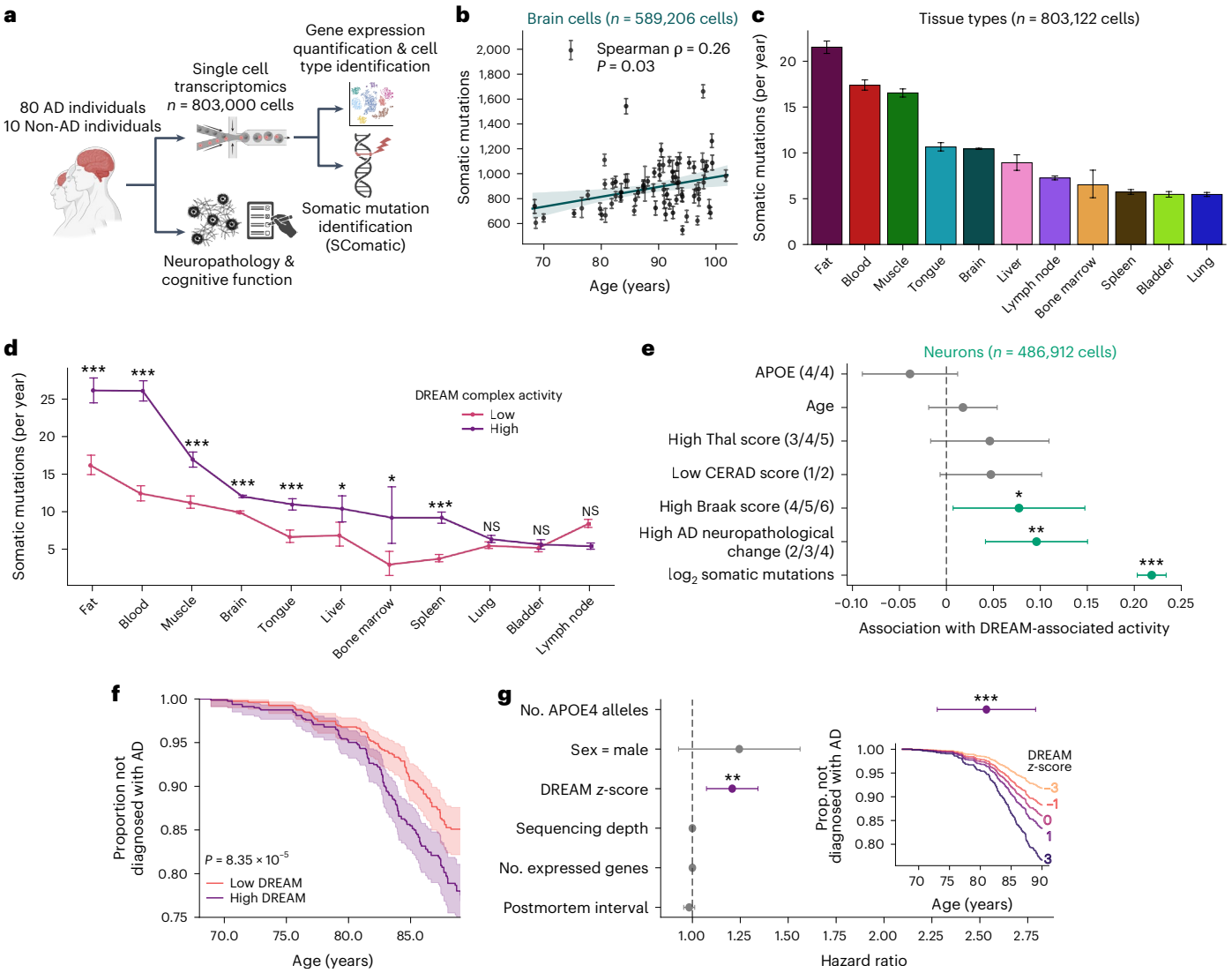

Fig. 5 | Multiple associations between DREAM-associated activity and Alzheimer's disease. a, 90 human individuals (80 with AD or neurodegeneration and 10 cognitively healthy) were profiled for mRNA expression in single cells from 11 tissues ($n = 803,122$ total cells, 73% of cells were from the brain) as well as neuropathology and cognitive function. Cell type and somatic mutation profile of each cell were identified from the single-cell mRNA. Panel **a** created in BioRender; Koch, Z. https://biorender.com/l31n122 (2026). **b**, Scatter-plot of the number of somatic mutations per haploid genome (Methods) identified in the brain of each individual, compared to the age of that individual ($n = 77$ individuals with ≥5,000 sequenced brain cells, $n = 589,206$ cells). Points and error bars indicate the mean and 95% CI across all cells from an individual. Two-sided P value calculated by modeling Spearman ρ as a Student's t-test distribution. **c**, Barplot indicating the mean and 95% CI of the number of somatic mutations identified in each cell per year within each tissue type (normalized to haploid genome size, $n = 803,122$ cells, $n = 90$ individuals). **d**, Number of somatic mutations in each cell (normalized to haploid genome size, $n = 803,122$ cells, $n = 90$ individuals; Methods) stratified by DREAM complex activity (highest versus lowest 20% of DREAM-associated activity scores within each tissue). Points denote means and error bars 95% CIs. P values are from a one-sided Mann–Whitney U-test; $^{***}P < 5.0 \times 10^{-17}$, $^{*}P < 0.005$ (Bonferroni-corrected) and NS, $P \geq 0.005$. **e**, Association of cell or individual-level covariates with DREAM complex activity in neurons ($n = 486,912$ neurons, $n = 77$ individuals). Dots and whiskers indicate the coefficient and 95% CI from linear mixed-effects modeling (Methods). P values are from a two-sided t-test; $^{***}P < 5.0 \times 10^{-30}$, $^{**}P < 5.0 \times 10^{-4}$, $^{*}P < 0.05$. Covariates with insignificant associations are shown in gray. **f**, Kaplan–Meier survival curve comparing the age at AD diagnosis between individuals with the top and bottom third of DREAM complex activities (purple versus pink, $n = 1,101$ individuals). The dark line and shaded area indicate the proportion of individuals without AD at a particular age and the 95% CI of this estimate, respectively. P value calculated using a two-sided log-rank test. **g**, Dot-and-whisker plot indicating the association of each variable on the y axis with age at AD diagnosis ($n = 1,101$ individuals). Dots and whiskers indicate the hazard ratio and 95% CIs from a Cox proportional hazard model (Methods). Asterisks indicate P values from a two-sided Wald test; $^{***}P < 5.0 \times 10^{-10}$, $^{**}P < 0.01$. Covariates with insignificant associations are shown in gray. Inset shows line plot of the predicted effect of different levels of DREAM on age at AD diagnosis, holding other factors constant.

(Fig. 6e,f). The ID mutational spectra also shifted: the prevalence of the ID21 mutational signature (2–4 bp deletions in double-repeats) was significantly reduced in DREAM LoF brains, whereas ID23 (1 bp deletions at homopolymer runs) was increased (Fig. 6g). Together, these results indicated that loss of DREAM activity reduces the lifetime accrual of somatic mutations, spanning multiple mutation types and mutational processes.

Discussion

Collectively, our results reveal a consistent set of associations suggesting that the DREAM complex may play a pivotal role in modulating the rate of DNA damage accumulation, thereby shaping organismal lifespan and the onset of aging-related pathologies (Fig. 6h). Consistent with a causal role, genetic disruption of DREAM assembly protects mice from somatic mutation, directly linking DREAM activity to mutation

https://doi.org/10.1038/s43587-026-01132-z

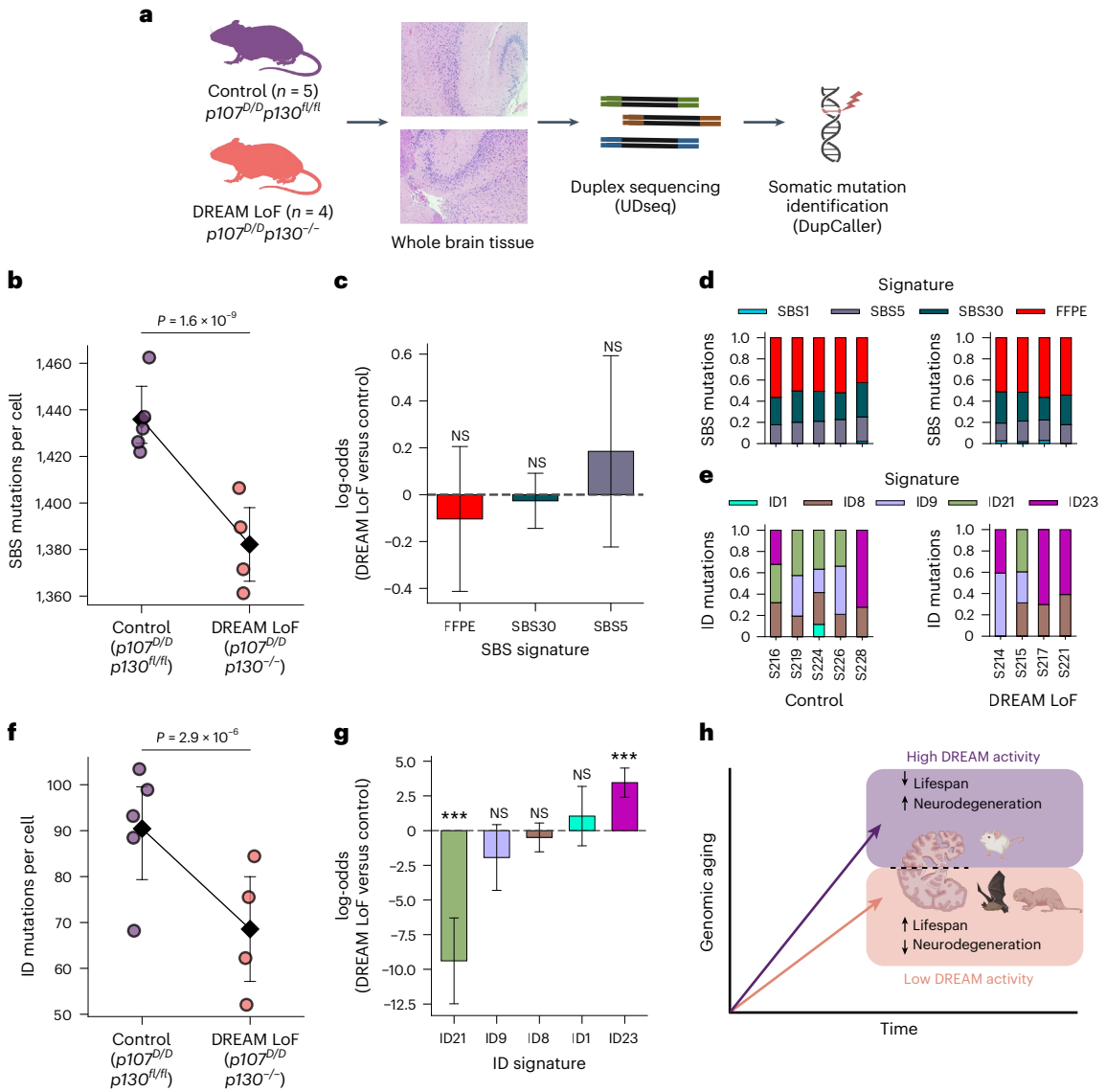

Fig. 6 | Reduced mutagenesis in brains of DREAM loss-of-function mice. **a**, Whole brain tissue slices were collected from control mice ($p107^{D/D}p130^{fl/fl}$, $n = 5$) or DREAM LoF mice ($p107^{D/D}p130^{-/-}$, $n = 4$). Somatic mutations were identified via duplex sequencing (UDseq) and somatic variant calling (DupCaller). Hematoxylin and eosin stains are shown for illustration purposes only. Panel **a** created in BioRender; Koch, Z. https://biorender.com/ley1ouq (2026). **b**, SBS mutations per (diploid) cell in each mouse. Points are individuals ($n = 4$ DREAM LoF mice; $n = 5$ control mice); diamonds and whiskers denote mean and 95% CI. Two-sided *P* value reflects the association between DREAM status and the count of SBS mutations per cell according to a negative binomial regression model (Methods). **c**, log-odds of each SBS signature in DREAM LoF versus control mice. Bar height denotes log-odds and error bars indicate 95% CI. *P* values indicate significance of association between DREAM status and the proportion of mutations assigned to each signature from a two-sided binomial model (Methods). NS, $P > 0.05$. **d**,**e**, Proportional contributions of SBS signatures (**d**) and ID signatures (colored stacked bars) (**e**) in each control or DREAM LoF mouse (*x* axis). The tissue preservation process (FFPE) is associated with a distinct SBS mutational signature. **f**, Similar to **b**, but showing ID mutations ($n = 4$ DREAM LoF mice; $n = 5$ control mice). Diamonds and whiskers denote the means and 95% CI. **g**, Similar to **c**, but for ID mutational signatures. $^{***}P < 5.0 \times 10^{-9}$, NS, $P > 0.05$. Bar height denotes log-odds and error bars indicate 95% CI. **h**, Model for the relationship between DREAM activity and aging phenotypes, in which higher DREAM activity associates with a faster rate of genomic aging due to repression of DNA repair. Consistent with this model, short lived species have higher DREAM activity than long-lived species and individuals with higher DREAM complex activity have accelerated neurodegeneration. Panel **h** created in BioRender; Koch, Z. https://biorender.com/khetvop (2026).

accumulation in vivo (Fig. 6). These results corroborate, and may help explain, previous research demonstrating that long-lived species and centenarians possess mechanisms enhancing genomic stability[6,10–12].

The simplest interpretation of our findings is that when the DREAM complex represses DNA repair, DNA damage tends to remain unresolved leading to somatic mutation and other consequences. Some of our experimental data indeed support this model: for instance, loss of DREAM reduced both SBS and ID mutation rates and reshaped the ID mutational spectrum (Fig. 6, reducing signature ID21, ref. 46) consistent with enhanced repair of replication-slippage intermediates. Furthermore, DREAM-target genes include those involved in nearly every major DNA repair pathway[23,24], including MUTYH, NEIL3 and POLD1 (base-excision repair[47,48]); RAD51, XRCC2 and BRCA2 (homologous recombination[49]); XRCC4, PARG and MRE11 (nonhomologous end joining[50]); and POLQ, PCNA and USP1 (translesion synthesis[51]). Simultaneously, unrepaired lesions can give rise to mutations by multiple mechanisms, such as cytosine deamination in the case of UV-induced cyclobutane pyrimidine dimers[52], mispairing of oxidized bases during

DNA replication[53,54] and error-prone translesion synthesis at replication forks stalled by DNA damage[55]. Nonetheless, this DREAM-mediated repression of DNA repair certainly operates alongside the other multifactorial determinants of mutation rate (Supplementary Note 1), including transcriptional activity, environmental exposure and chromatin context. Taken together, these observations suggest that by reducing the expression of DNA repair factors, the DREAM complex allows DNA damage to persist, thereby increasing the likelihood that unrepaired lesions will be converted into permanent mutations through replication or error-prone repair processes.

Our inducible DREAM loss-of-function experiment provides causal support for DREAM influencing mutation accumulation. Notably, the magnitude of this effect was modest (4% reduction in SBS and ~20% reduction in ID mutations in brain; Fig. 6) compared to the difference seen in brain cells profiled for DREAM-associated activity and mutation burden using scRNA-seq (~twofold difference between low versus high DREAM cells; Fig. 2). This disparity may be due to differences in (1) the mutation detection method (ultra-accurate duplex sequencing of DNA versus mutation calling from transcribed sequences in single-cell RNA); (2) the representation of cell types measured; and (3) cohort and study design (mouse strain, age, and so on). Nonetheless, all analyses share the same directional conclusion that greater DREAM activity is tied to faster somatic mutation rates.

Long-lived species exhibit a range of adaptations thought to underlie their extended lifespans, including enhanced DNA repair capacities[2], reduced somatic mutation rates[4,5], altered metabolic rates[56] and larger body sizes[57]. We observed an inverse association between DREAM complex-associated activity and species lifespan (Fig. 3), which may be either a cause or result of such adaptations. By permitting increased expression of DNA repair genes, reduced DREAM activity in long-lived species could plausibly enhance DNA repair and decrease somatic mutation rates. This idea aligns with reports of elevated expression of DNA repair genes in long-lived species[58,59], although structural modifications to the repair factors themselves have also been implicated in such heightened repair capabilities[6]. Alternatively, reduced DREAM activity may be a downstream effect of other adaptations that more directly confer extended longevity. Although the observed relationship between DREAM-associated activity and lifespan does not seem to be confounded by species size (Fig. 3d and Extended Data Fig. 4a,b), the possibility of other confounding factors, such as lower metabolic rate, difference in cell turnover, chromatin organization or additional, yet unidentified mechanisms, warrants further investigation.

Within species, we found that elevated DREAM-associated activity corresponded to both decreased survival of mice fed an HFD (Fig. 4) and earlier onset of AD in humans (Fig. 5), a pattern potentially explained by heightened genomic damage. Indeed, high DREAM-associated activity correlated with greater somatic mutation burdens and more severe neuropathology, aligning with previous evidence implicating DNA damage in age-related diseases[60–62] in general and in AD[63,64] in particular. Nevertheless, we cannot exclude the possibility that in these cases DREAM-associated activity is merely a marker of other processes that drive morbidity and mortality, rather than a direct cause.

Extrapolating from these findings, DREAM inhibition could represent a new therapeutic approach to prevent or mitigate DNA damage-driven conditions, including aging. Compounds that disrupt DREAM complex formation[23,65,66] have already shown beneficial effects in model organisms, reducing oxidative stress[67], preserving bone density[68], enhancing insulin sensitivity[69,70] and improving cognitive function[71]. Our results suggest that the upregulation of DNA repair brought about by these DREAM-inhibiting compounds may underlie their therapeutic benefits. While some of these compounds are in early development for human neurological disorders[72,73], the link between DREAM activity and DNA repair explored here points to a broader opportunity to use DREAM-modulating therapies to slow or prevent age-related pathologies in humans.

Methods

This research complies with all relevant ethical regulations. Animal experiments involving DREAM loss-of-function mice were approved by the Animal Use Subcommittee at Western University.

scRNA-seq processing

Each scRNA-seq dataset was processed separately using Scanpy[74]. First, any cell with fewer than 200 detected genes or more than 10,000,000 total read counts was removed. Second, any gene detected in fewer than three cells was discarded (using the Scanpy functions 'filter_cells' and 'filter_genes'). Third, the total read count within each cell was normalized to 10,000 ('normalize_per_cell'), log-scaled ('log1p') and then scaled to have a value between zero and ten ('scale').

Calculation of DREAM-associated activity

DREAM-regulated genes (n = 328 genes) were defined as genes with promoters concurrently bound by at least three core DREAM complex subunits in a ChIP–seq experiment targeting LIN9, LIN54, p130 and E2F4 in quiescent human cells[24]. The promoter of a gene was determined to be 'bound' by a DREAM subunit if a ChIP–seq peak corresponding to that subunit was found within ±1 kb of the transcription start site of that gene. The single-sample gene set enrichment analysis (ssGSEA[75]) of the expression of these genes was calculated in each RNA-seq or scRNA-seq sample. For datasets in which the expression of one or more DREAM-target genes was not detected, the remaining genes were used in the ssGSEA calculation. The ssGSEA 'normalized enrichment score' was regressed against the number of expressed genes and total count of reads in each cell or sample, to correct for technical variation arising from sequencing depth[76]. The residuals from this regression (the normalized enrichment score corrected for sequencing depth) were inverted and scaled to be positive, making higher scores correspond to greater DREAM activity (lower expression of DREAM-regulated genes). The resulting value was termed 'DREAM-associated activity' (Fig. 1).

Calculation of alternative pathway activity scores

The same activity calculation method detailed above was applied to four alternative DREAM-target gene sets and six gene sets representing the target genes of DREAM-related cell-cycle and chromatin-remodeling pathways (Extended Data Fig. 2, complete lists of genes can be found in Supplementary Table 2): 'DREAM Expanded (Litovchick),' the set of DREAM-target genes defined by Litovchik et al.[24], consisting of all genes where ChIP–seq of quiescent human cells indicated that ≥3 DREAM subunits were found to be bound within −8.5 kb and +2 kb of the gene's promoter (n = 788); 'DREAM Expanded (Fischer),' a manually curated set of DREAM-target genes from Fischer et al.[77] (n = 969); 'DREAM DR,' a subset of the primary 328-gene DREAM gene set including only DNA repair genes, as annotated by Bujarrabal-Dueso et al.[23] (n = 67); 'DREAM Other,' all genes in the main 328-gene DREAM gene set not annotated to be DNA repair genes (n = 261); 'p53,' the set of p53 target genes defined by Fischer et al.[77] (n = 311); 'MMB-FOXM1,' the set of MMB-FOXM1 target genes defined by Fischer et al.[77] (n = 282); 'RB-E2F,' the set of RB-E2F target genes defined by Fischer et al.[77] (n = 506); 'E2F7,' the set of E2F7 target genes defined by Westendorp et al.[78] (n = 89); 'FOXM1,' the FOXM1_01 gene set from MSigDB[79] (n = 248); and 'DNMT1,' the JACKSON_DNMT1_TARGETS_UP gene set from MSigDB[79] (n = 81).

Proteomic DREAM-associated activity validation

Matched transcriptomic and proteomic data from the Clinical Proteomic Tumor Analysis Consortium[80] were used to compare the transcriptomic DREAM-associated activity score with the abundance and phosphorylation state of LIN52 and p107 (RBL1). A total of 160 individuals were included from the clear cell renal cell carcinoma and head and neck squamous cell carcinoma cohorts; samples in which the DREAM components were not detected were excluded. Multivariate linear regression was performed using the model:

$$\text{DREAM activity} \sim \text{tissue type} + \text{LIN52} + \text{p107} + \text{LIN52}_{\text{s28 phosphorylation}} + \text{p107}_{\text{phosphorylation}}$$

where $\text{p107}_{\text{phosphorylation}}$ is the mean phosphorylation across 17 detected phospho-sites on p107.

Identification of somatic mutations in scRNA-seq

For the Tabula Sapiens[39] and SEA-AD[81] scRNA-seq/single-nucleotide (sn)RNA-seq datasets, SComatic[38] was applied with default parameters to identify somatic single-nucleotide substitution mutations. In brief, first somatic mutations in each 'pseudo-bulked' cell type in each individual were identified, treating variants present in more than one cell type as germline. Second, somatic mutations in each individual cell were identified and filtered to include only variants also identified at the 'pseudo-bulk' level of the respective cell type. Third, the count of somatic mutations in each cell was divided by the number of base pairs from which mutations were called in that cell (owing to there being sufficient coverage at these loci), to define the somatic mutation rate per base pair. Cells without sufficient coverage for mutation identification in greater than 10 kb were discarded. The approximate number of somatic mutations per cell was then calculated by multiplying the somatic mutation rate per base pair by the approximate number of base pairs in the haploid human genome (3.0×10^9). Finally, the somatic mutation rate per cell per year was calculated by dividing the number of somatic mutations per cell by the age of the donor of that cell. For the TMS dataset, somatic mutations had been identified by the original publication[30], and we simply scaled these somatic mutation burdens to be relative to the number of bases from which mutations were called.

Somatic mutation rate validation

The somatic mutation rate per kb per month, estimated from scRNA-seq in mouse skin cells (Fig. 2), was compared to a previous estimate of somatic mutation rates in mouse fibroblasts[7] obtained using the single-cell multiple displacement amplification DNA sequencing method[82]. Milholland et al.[7] found there to be approximately 4.4×10^{-7} somatic mutations per bp in a 5-day-old mouse. We converted this estimate to be in units of mutations per kb per month, using the average month length of 30.44 days, and found our estimate of 0.0030 mutations per kb per month to be remarkably similar to this previous estimate of 0.0027 mutations per kb per month.

$$\frac{4.4 \times 10^{-7}\ \text{mutations}}{5\ \text{days} \times 1\ \text{bp}} \times \frac{30.437\ \text{days}}{1\ \text{month}} \times \frac{1{,}000\ \text{bp}}{1\ \text{kb}} = 0.0027$$

We also compared the mutation rates we identified from human sc/snRNA-seq (Fig. 5) to previous estimates based on DNA sequencing of the same or similar cell types as those considered in our analyses. This included seven estimates of mutation rates in immune cells[83–86], three in neurons[22,83,87,88] and one in each of muscle satellite cells[89], skin fibroblasts[90] and cells from the bladder urothelium[83,88]. DNA- and RNA-based mutation estimates were generally consistent though the rates we now observed were marginally lower (Extended Data Fig. 7b–f). This difference in mutation rates may reflect that RNA, unlike previous measures from DNA, is primarily derived from coding sequences, which have reduced somatic mutation rates relative to noncoding sequences owing to increased mismatch and transcription-coupled repair[8,88,91,92].

Generation of random background distributions

To serve as background distributions for the association of DREAM-associated activity with somatic mutation rate (Fig. 2g,h), species maximum lifespan (Fig. 4c), and age at AD onset (Extended Data Fig. 7h,i), the association between the expression of random gene sets and these measures was calculated. In each dataset, 500–1,000 sets of genes were randomly selected, with replacement, from all genes detected in that dataset. A gene was available for selection in a random gene set for a particular dataset if (1) it had nonzero expression in at least one cell or sample in that dataset; and (2) passed quality control filters (see 'scRNA-seq processing' section). The number of genes in each of these random sets was defined to be the same as the number of DREAM-target genes detected in that dataset ($n = 249$ for the TMS mouse scRNA-seq, $n = 308$ for the cross-species RNA-seq dataset and $n = 322$ for the ROSMAP human brain RNA-seq). The 'activity' of these random gene sets was then calculated by treating these genes as if they were DREAM-target genes and applying the process that was used to calculate DREAM-associated activity (ssGSEA followed by sequencing depth correction and inversion, see the 'Calculation of DREAM-associated activity' Methods section). Finally, the activity of these random gene sets was compared to the respective measures of interest and the strength of that association was contrasted to that of DREAM-associated activity and the measure of interest.

Comparison of lifespan across species

Cross-species comparisons of DREAM-associated activity, maximum lifespan, adult weight and somatic mutation rate were conducted using a dataset of gene expression data (RNA-seq) collected from three tissues (brain, liver and kidney) of 92 different species[32] ($n = \sim 3$ samples per species per tissue, $n = 803$ total samples). We first calculated a representative DREAM-associated activity for each species in each tissue by averaging the DREAM-associated activity scores of all individuals of a given species in a tissue. Species with fewer than two sampled individuals in a given tissue were discarded from comparisons considering that tissue; taxonomic orders with only a single sampled species were discarded. We examined the association of DREAM-associated activity with maximum lifespan using zero-intercept reduced major axis regression (implemented by the pylr2 regress2 function[93]), in each tissue separately (Fig. 4b,c). Because body size can confound interspecies lifespan relationships[94], we conducted the same DREAM versus maximum lifespan comparison but correcting for adult weight. To do so, we performed an allometric regression of each trait (DREAM-associated activity and maximum lifespan) on $\log_{10}$-transformed adult weight and compared the resulting residuals (partial regression of DREAM-associated activity versus maximum lifespan with respect to adult weight, Fig. 5d and Extended Data Fig. 4a,b). Finally, integrating a previously published estimate of somatic mutation rates[4] for a subset of the same species, we performed analogous cross-species comparisons of DREAM complex activity and somatic mutation rate, both with and without adjusting for adult weight (Fig. 4f and Extended Data Fig. 4c–g).

Survival analysis of mouse strains

The Williams et al.[37] dataset consists of 50 distinct strains of inbred mice split into two cohorts: the 'Deeply Profiled Cohort,' which was profiled for liver gene expression (RNA-seq), blood biomarkers and the weight of different organs ($n = 270$ mice); and the 'Lifespan Cohort,' which was followed to measure the lifespan of each strain ($n = 612$ mice). The DREAM-associated activity of each mouse in the Deeply Profiled Cohort was calculated from the liver RNA-seq. Four strains with highly variable DREAM-associated activity scores across mice were removed (s.d. > 0.2). The Deeply Profiled Cohort was used to estimate strain-specific covariates for use in a Cox proportional hazards model (lifelines CoxPHFitter[95]). This model was fit to the survival data of the Lifespan Cohort to measure the association of lifespan with diet (HFD versus CD), DREAM-associated activity, weight, clinical biomarkers and weight change (Fig. 4).

$$\text{survival} \sim \text{diet} \times (\text{DREAM activity} + \text{PC1}_{\text{weight \& blood lipids}} + \text{seq. depth} + \Delta\text{weight})$$

Covariates in the Cox model included: the mean DREAM-associated activity value within each strain on each diet; the mean

sequencing depth in each strain, to account for any confounding of DREAM-associated activity by differences in sequencing depth between strains; the first principal component (PC1, 25.2% of variance explained; Extended Data Fig. 6g) from an analysis of normalized clinical biomarkers and organ weights (variables listed in Extended Data Fig. 6g); diet group (CD or HFD); and change in body weight since starting the respective diet.

Neuropathology versus DREAM-associated activity

Neurodegenerative pathology was compared to DREAM complex activity using the SEA-AD[81] dataset, in which snRNA-seq was carried out on 803,112 brain cells from 83 individuals. Neuropathological assessments, including Thal phase, CERAD (Consortium to Establish a Registry for Alzheimer's Disease) score and Braak stage, had been conducted for each individual and integrated into an overall ADNC score[96]. Each variable was binarized into high (Thal ≥ 3, CERAD ≤ 2, Braak ≥ 4 and ADNC ≥ 2) versus low AD risk. Then, linear mixed-effects regression was used to test the association between each of these variables (in addition to APOE 4/4 genotype, age (scaled to units of decades) and the count of somatic mutations per cell ($\log_2$ scaled)) and DREAM-associated activity (Fig. 5e). These variables were treated as fixed effects, whereas the individual identifier was modeled as a random effect, to account for the nested structure of the data, with multiple cells sampled per individual.

Association of DREAM-associated activity with age at AD diagnosis

The ROSMAP[41] dataset was used to investigate the association of DREAM-associated activity with the diagnosis of AD. In this study, RNA-seq data were collected from multiple brain regions (dorsolateral prefrontal cortex, head of the caudate nucleus, posterior cingulate cortex, temporal cortex and frontal cortex) of deceased donors (mean ± s.d. of 2.4 ± 1.0 brain regions per individual, n = 1,105 individuals, n = 2,776 samples). A Cox proportional hazard model (lifelines CoxPHFitter[95]) was fit to predict the age at AD diagnosis of these individuals. Age at AD diagnosis was right-censored at 90 years to ensure masking of donor identity. The DREAM-associated activity, number of APOE 4 alleles, sex, total RNA sequencing depth, count of genes with detected expression and the duration of time between death and tissue procurement (postmortem interval) were used as covariates in the model. DREAM-associated activity scores were z-score-normalized within each brain region and outliers were dropped (samples with DREAM $|z| > 5$). As there were multiple samples from each individual, the model was corrected for intra-individual correlations through clustered variance adjustment (Fig. 5f,g).

DREAM-deficient mice

We leveraged a previous study[42] that had engineered mice (Jackson Laboratory stock 008177) with inactivated DREAM activity. In these mice, DREAM assembly was prevented by combining a constitutive *Rbl1* missense allele ($p107^{D/D}$), which disrupts MuvB binding, with tamoxifen-induced UBC-Cre-ERT2 deletion of *Rbl2*. Because either p107 or p130 can scaffold DREAM, loss of p130 in the $p107^{D/D}$ background abolishes assembly of the complex[42]. Control mice were Cre-negative. At 8 weeks of age, both groups were treated with tamoxifen, which activated the deletion of the gene encoding p130 (*Rbl2*), producing DREAM LoF mice ($p107^{D/D}p130^{-/-}$, n = 5), while the control mice retained intact DREAM activity due to Cre-negativity ($p107^{D/D}p130^{fl/fl}$, n = 5). Brain tissue was obtained from these mice at death, formalin-fixed and paraffin-embedded. Animal experiments involving DREAM LoF mice were approved by the Animal Use Subcommittee at Western University.

Duplex sequencing (UDSeq) library preparation and sequencing

FFPE mouse brain tissues (n = 10) were sectioned, stained with hematoxylin and eosin, and punches containing sufficient nuclei were selected by microscopic inspection. Genomic DNA was extracted using the QIAamp DNA FFPE Advanced kit (QIAGEN, cat. no. 56704) according to the manufacturer's instructions and quantified by Qubit, with 500 ng per sample normalized to 5 ng μl^{-1} for library preparation. Genomic DNA was enzymatically fragmented using the UltraShear system (M7634L) for 25 min, targeting an average fragment size of approximately 350 bp. The fragmented DNA was then processed using the UDSeq[97] library preparation workflow with the xGen cfDNA and FFPE DNA Library Preparation kit. All steps were performed on magnetic beads to minimize DNA loss during purification and enhance library conversion efficiency. For final library construction, 0.175 fmol of UMI-ligated DNA were amplified via 15 cycles of PCR to incorporate Illumina-compatible dual index sequences. For matched healthy samples, 5 fmol of UMI-ligated DNA from the same source were amplified using ten PCR cycles. The resulting universal dual-indexed libraries were sequenced at the UCSD IGM Genomics Center using a 25B flow cell on the NovaSeq X platform.

Identification of somatic mutations in duplex sequencing data

Sequencing data were downloaded and analyzed within the Triton Shared Computing Cluster at the San Diego Supercomputer Center (https://doi.org/10.57873/T34W2R). Somatic mutation calling and mutational burden analysis were performed using DupCaller 1 (v.1.0.1)[98] on UDSeq data with matched healthy samples. Variant Call Format files generated by DupCaller were used for mutational profiling and signature assignment, following our previously established methodology using the SigProfiler suite of tools. In particular, SigProfilerAssignment was run on the variant call set, with the entire mouse COSMIC catalog and FFPE signature from Guo et al.[44] FFPE signature as the input signatures. Mutations classified as FFPE artifacts were discarded and remaining mutations were analyzed. For each sample, the raw mutation count in the sequenced bases was extrapolated to estimate the number of mutations expected if the entire diploid genome had been covered at sufficient depth, yielding a per-cell equivalent mutation burden (termed 'mutations per cell').

Analysis of UDseq mutation calls

Negative binomial regression models were used to test for a difference in frequency of single-base substitutions and insertion/deletion mutations between DREAM LoF and control mice. Models of three complexities were compared:

(Model 1) mutation count

~ DREAM status + genomic coverage + read families

(Model 2) mutation count

~ DREAM status + genomic coverage + read families + age

(Model 3) mutation count

~ DREAM status + genomic coverage × read families + age

Model 3 showed the best fit across all mutation types as measured by log-likelihood (Extended Data Fig. 8a–f) and was therefore used for all statistical comparisons of mutation frequency. For comparisons of the proportional contribution of mutational processes, a binomial model of the same form was used. One outlier sample (identified by having a Cook's distance[99,100] >1 and total mutation count $|z$-score$| > 3$ across both mutation classes) was removed (Extended Data Fig. 8g–i).

Software

All analyses were performed in Python v.3.10. Data analysis was conducted using Pandas v.1.5.3, SciPy v.1.10.0, Pingouin v.0.5.3 and Statsmodels v.0.13.5. Data were visualized with Seaborn v.0.12.1 and Matplotlib v.3.7.1.

Statistics and reproducibility

No statistical method was used to predetermine sample size and the investigators were not blinded to allocation during experiments and outcome assessment. Random sampling with replacement was used in the generation of null distributions for statistical testing, whereby gene sets of matched size were repeatedly drawn from the pool of expressed genes to construct empirical background distributions. Specific statistical approaches used are noted in the respective Methods sections and figure captions. Data distribution was assumed to be normal but this was not formally tested.

Reporting summary

Further information on research design is available in the Nature Portfolio Reporting Summary linked to this article.

Data availability

Raw UD-sequencing data can be accessed on the Sequence Read Archive under BioProject accession no. PRJNA1436559. Other data can be accessed through the respective publications (Supplementary Table 1).

Code availability

All custom algorithms and analysis code are available in the GitHub repository at https://github.com/zanekoch/dream_proj.

References

1. Kratz, A. et al. A multi-scale map of protein assemblies in the DNA damage response. *Cell Syst.* **14**, 447–463.e8 (2023).
2. Harper, J. M., Salmon, A. B., Leiser, S. F., Galecki, A. T. & Miller, R. A. Skin-derived fibroblasts from long-lived species are resistant to some, but not all, lethal stresses and to the mitochondrial inhibitor rotenone. *Aging Cell* **6**, 1–13 (2007).
3. Ma, S. et al. Cell culture-based profiling across mammals reveals DNA repair and metabolism as determinants of species longevity. *eLife* https://doi.org/10.7554/elife.19130 (2016).
4. Cagan, A. et al. Somatic mutation rates scale with lifespan across mammals. *Nature* **604**, 517–524 (2022).
5. Zhang, L. et al. Maintenance of genome sequence integrity in long- and short-lived rodent species. *Sci. Adv.* **7**, eabj3284 (2021).
6. Tian, X. et al. SIRT6 is responsible for more efficient DNA double-strand break repair in long-lived species. *Cell* **177**, 622–638.e22 (2019).
7. Milholland, B. et al. Differences between germline and somatic mutation rates in humans and mice. *Nat. Commun.* **8**, 15183 (2017).
8. Moore, L. et al. The mutational landscape of human somatic and germline cells. *Nature* **597**, 381–386 (2021).
9. Lynch, M. Evolution of the mutation rate. *Trends Genet.* **26**, 345–352 (2010).
10. Sebastiani, P. et al. Genetic signatures of exceptional longevity in humans. *PLoS ONE* **7**, e29848 (2012).
11. Gurinovich, A. et al. Effect of longevity genetic variants on the molecular aging rate. *GeroScience* **43**, 1237–1251 (2021).
12. Simon, M. et al. A rare human centenarian variant of SIRT6 enhances genome stability and interaction with Lamin A. *EMBO J.* **41**, e110393 (2022).
13. López-Otín, C., Blasco, M. A., Partridge, L., Serrano, M. & Kroemer, G. Hallmarks of aging: an expanding universe. *Cell* **186**, 243–278 (2023).
14. Schumacher, B., Pothof, J., Vijg, J. & Hoeijmakers, J. H. J. The central role of DNA damage in the ageing process. *Nature* **592**, 695–703 (2021).
15. Arvanitaki, E. S. et al. Microglia-derived extracellular vesicles trigger age-related neurodegeneration upon DNA damage. *Proc. Natl Acad. Sci. USA* **121**, e2317402121 (2024).
16. Yousefzadeh, M. J. et al. Failure to repair endogenous DNA damage in β-cells causes adult-onset diabetes in mice. *Aging Biol.* https://doi.org/10.59368/agingbio.20230015 (2023).
17. Yoshimoto, N. et al. Significance of podocyte DNA damage and glomerular DNA methylation in CKD patients with proteinuria. *Hypertens. Res.* **46**, 1000–1008 (2023).
18. Hishikawa, A. et al. DNA damage and expression of DNA methylation modulators in urine-derived cells of patients with hypertension and diabetes. *Sci. Rep.* **10**, 3377 (2020).
19. Nelson, T. J. & Xu, Y. Sting and p53 DNA repair pathways are compromised in Alzheimer's disease. *Sci. Rep.* **13**, 8304 (2023).
20. Zhao, H., Wang, S. & Li, X. DNA damage accumulation in aging brain and its links to Alzheimer's disease progression. *Genome Instability Dis.* **3**, 172–178 (2022).
21. Wyss-Coray, T. Ageing, neurodegeneration and brain rejuvenation. *Nature* **539**, 180–186 (2016).
22. Miller, M. B. et al. Somatic genomic changes in single Alzheimer's disease neurons. *Nature* **604**, 714–722 (2022).
23. Bujarrabal-Dueso, A. et al. The DREAM complex functions as conserved master regulator of somatic DNA-repair capacities. *Nat. Struct. Mol. Biol.* **30**, 475–488 (2023).
24. Litovchick, L. et al. Evolutionarily conserved multisubunit RBL2/p130 and E2F4 protein complex represses human cell cycle-dependent genes in quiescence. *Mol. Cell* **26**, 539–551 (2007).
25. Litovchick, L., Florens, L. A., Swanson, S. K., Washburn, M. P. & DeCaprio, J. A. DYRK1A protein kinase promotes quiescence and senescence through DREAM complex assembly. *Genes Dev.* **25**, 801–813 (2011).
26. Sadasivam, S. & DeCaprio, J. A. The DREAM complex: master coordinator of cell cycle-dependent gene expression. *Nat. Rev. Cancer* **13**, 585–595 (2013).
27. Engeland, K. Cell cycle arrest through indirect transcriptional repression by p53: I have a DREAM. *Cell Death Differ.* **25**, 114–132 (2018).
28. Guiley, K. Z. et al. Structural mechanisms of DREAM complex assembly and regulation. *Genes Dev.* **29**, 961–974 (2015).
29. Kandhaya-Pillai, R. et al. Key elements of cellular senescence involve transcriptional repression of mitotic and DNA repair genes through the p53-p16/RB-E2F-DREAM complex. *Aging* **15**, 4012–4034 (2023).
30. Tabula Muris Consortium A single-cell transcriptomic atlas characterizes ageing tissues in the mouse. *Nature* **583**, 590–595 (2020).
31. Picelli, S. et al. Smart-seq2 for sensitive full-length transcriptome profiling in single cells. *Nat. Methods* **10**, 1096–1098 (2013).
32. Liu, W. et al. Large-scale across species transcriptomic analysis identifies genetic selection signatures associated with longevity in mammals. *EMBO J.* **42**, e112740 (2023).
33. Yuzefovych, L. V., Musiyenko, S. I., Wilson, G. L. & Rachek, L. I. Mitochondrial DNA damage and dysfunction, and oxidative stress are associated with endoplasmic reticulum stress, protein degradation and apoptosis in high fat diet-induced insulin resistance mice. *PLoS ONE* **8**, e54059 (2013).
34. de Assis, A. M. et al. High fat and highly thermolyzed fat diets promote insulin resistance and increase DNA damage in rats. *Exp. Biol. Med.* **234**, 1296–1304 (2009).
35. Włodarczyk, M., Jabłonowska-Lietz, B., Olejarz, W. & Nowicka, G. Anthropometric and dietary factors as predictors of DNA damage in obese women. *Nutrients* **10**, 578 (2018).
36. Kompella, P. et al. Obesity increases genomic instability at DNA repeat-mediated endogenous mutation hotspots. *Nat. Commun.* **15**, 6213 (2024).
37. Williams, E. G. et al. Multiomic profiling of the liver across diets and age in a diverse mouse population. *Cell Syst.* **13**, 43–57.e6 (2022).

38. Muyas, F. et al. De novo detection of somatic mutations in high-throughput single-cell profiling data sets. *Nat. Biotechnol.* https://doi.org/10.1038/s41587-023-01863-z (2023).
39. Tabula Sapiens Consortium* et al. The Tabula Sapiens: A multiple-organ, single-cell transcriptomic atlas of humans. *Science* **376**, eabl4896 (2022).
40. Gabitto, M. I. et al. Integrated multimodal cell atlas of Alzheimer's disease. *Nat. Neurosci.* **27**, 2366–2383 (2024).
41. De Jager, P. L. et al. A multi-omic atlas of the human frontal cortex for aging and Alzheimer's disease research. *Sci Data* **5**, 180142 (2018).
42. Perampalam, P. et al. Disrupting the DREAM transcriptional repressor complex induces apolipoprotein overexpression and systemic amyloidosis in mice. *J. Clin. Invest*. https://doi.org/10.1172/jci140903 (2021).
43. Alexandrov, L. B. et al. Signatures of mutational processes in human cancer. *Nature* **500**, 415–421 (2013).
44. Guo, Q. et al. The mutational signatures of formalin fixation on the human genome. *Nat. Commun.* **13**, 4487 (2022).
45. Alexandrov, L. B. et al. Clock-like mutational processes in human somatic cells. *Nat. Genet.* **47**, 1402–1407 (2015).
46. Everall, A. et al. Comprehensive repertoire of the chromosomal alteration and mutational signatures across 16 cancer types from 10,983 cancer patients. Preprint at *bioRxiv* https://doi.org/10.1101/2023.06.07.23290970 (2023).
47. Krokan, H. E. & Bjørås, M. Base excision repair. *Cold Spring Harb. Perspect. Biol.* **5**, a012583 (2013).
48. Nicolas, E., Golemis, E. A. & Arora, S. POLD1: Central mediator of DNA replication and repair, and implication in cancer and other pathologies. *Gene* **590**, 128–141 (2016).
49. Clauson, C., Schärer, O. D. & Niedernhofer, L. Advances in understanding the complex mechanisms of DNA interstrand cross-link repair. *Cold Spring Harb. Perspect. Biol.* **5**, a012732 (2013).
50. Davis, A. J. & Chen, D. J. DNA double strand break repair via non-homologous end-joining. *Transl. Cancer Res.* **2**, 130–143 (2013).
51. Powers, K. T. & Washington, M. T. Eukaryotic translesion synthesis: choosing the right tool for the job. *DNA Repair* **71**, 127–134 (2018).
52. Mao, P., Wyrick, J. J., Roberts, S. A. & Smerdon, M. J. UV-induced DNA damage and mutagenesis in chromatin. *Photochem. Photobiol.* **93**, 216–228 (2017).
53. Sekiguchi, M. & Tsuzuki, T. Oxidative nucleotide damage: consequences and prevention. *Oncogene* **21**, 8895–8904 (2002).
54. Viel, A. et al. A specific mutational signature associated with DNA 8-oxoguanine persistence in MUTYH-defective colorectal cancer. *eBioMedicine* **20**, 39–49 (2017).
55. Zhang, H. Mechanisms of mutagenesis induced by DNA lesions: multiple factors affect mutations in translesion DNA synthesis. *Crit. Rev. Biochem. Mol. Biol.* **55**, 219–251 (2020).
56. Hulbert, A. J., Pamplona, R., Buffenstein, R. & Buttemer, W. A. Life and death: metabolic rate, membrane composition, and life span of animals. *Physiol. Rev.* **87**, 1175–1213 (2007).
57. Speakman, J. Body size, energy metabolism and lifespan. *J. Exp. Biol.* **208**, 1717–1730 (2005).
58. MacRae, S. L. et al. DNA repair in species with extreme lifespan differences. *Aging* **7**, 1171–1184 (2015).
59. Firsanov, D. et al. DNA repair and anti-cancer mechanisms in the long-lived bowhead whale. Preprint at *bioRxiv* https://doi.org/10.1101/2023.05.07.539748 (2024).
60. Tall, A. R. & Fuster, J. J. Clonal hematopoiesis in cardiovascular disease and therapeutic implications. *Nat. Cardiovasc. Res.* **1**, 116–124 (2022).
61. Jaiswal, S. et al. Clonal hematopoiesis and risk of atherosclerotic cardiovascular disease. *N. Engl. J. Med.* **377**, 111–121 (2017).
62. Zhao, Y., Simon, M., Seluanov, A. & Gorbunova, V. DNA damage and repair in age-related inflammation. *Nat. Rev. Immunol.* **23**, 75–89 (2023).
63. Lovell, M. A. & Markesbery, W. R. Oxidative DNA damage in mild cognitive impairment and late-stage Alzheimer's disease. *Nucleic Acids Res.* **35**, 7497–7504 (2007).
64. Asada-Utsugi, M. et al. Failure of DNA double-strand break repair by tau mediates Alzheimer's disease pathology in vitro. *Commun. Biol.* **5**, 358 (2022).
65. Ogawa, Y. et al. Development of a novel selective inhibitor of the Down syndrome-related kinase Dyrk1A. *Nat. Commun.* **1**, 86 (2010).
66. Seifert, A., Allan, L. A. & Clarke, P. R. DYRK1A phosphorylates caspase 9 at an inhibitory site and is potently inhibited in human cells by harmine. *FEBS J.* **275**, 6268–6280 (2008).
67. Réus, G. Z. et al. Harmine and imipramine promote antioxidant activities in prefrontal cortex and hippocampus. *Oxid. Med. Cell. Longev.* **3**, 325–331 (2010).
68. Caruso, A., Caira, V., El-Kashef, H. & Saturnino, C. The potential of indole alkaloids in bone health and osteoporosis management. *Appl. Sci.* **14**, 8124 (2024).
69. Waki, H. et al. The small molecule harmine is an antidiabetic cell-type-specific regulator of PPARγ expression. *Cell Metab.* **5**, 357–370 (2007).
70. Morsy, M. H. E., Nabil, Z. I., Darwish, S. T., Al-Eisa, R. A. & Mehana, A. E. Anti-diabetic and anti-adipogenic effect of harmine in high-fat-diet-induced diabetes in mice. *Life* https://doi.org/10.3390/life13081693 (2023).
71. Branca, C. et al. Dyrk1 inhibition improves Alzheimer's disease-like pathology. *Aging Cell* **16**, 1146–1154 (2017).
72. de la Torre, R. et al. Safety and efficacy of cognitive training plus epigallocatechin-3-gallate in young adults with Down's syndrome (TESDAD): a double-blind, randomised, placebo-controlled, phase 2 trial. *Lancet Neurol.* **15**, 801–810 (2016).
73. Stotani, S., Giordanetto, F. & Medda, F. DYRK1A inhibition as potential treatment for Alzheimer's disease. *Future Med. Chem.* **8**, 681–696 (2016).
74. Wolf, F. A., Angerer, P. & Theis, F. J. SCANPY: large-scale single-cell gene expression data analysis. *Genome Biol.* **19**, 15 (2018).
75. Subramanian, A. et al. Gene set enrichment analysis: a knowledge-based approach for interpreting genome-wide expression profiles. *Proc. Natl Acad. Sci. USA* **102**, 15545–15550 (2005).
76. Lause, J., Berens, P. & Kobak, D. Analytic Pearson residuals for normalization of single-cell RNA-seq UMI data. *Genome Biol.* **22**, 258 (2021).
77. Fischer, M., Grossmann, P., Padi, M. & DeCaprio, J. A. Integration of TP53, DREAM, MMB-FOXM1 and RB-E2F target gene analyses identifies cell cycle gene regulatory networks. *Nucleic Acids Res.* **44**, 6070–6086 (2016).
78. Westendorp, B. et al. E2F7 represses a network of oscillating cell cycle genes to control S-phase progression. *Nucleic Acids Res.* **40**, 3511–3523 (2012).
79. Liberzon, A. et al. Molecular signatures database (MSigDB) 3.0. *Bioinformatics* **27**, 1739–1740 (2011).
80. Li, Y. et al. Proteogenomic data and resources for pan-cancer analysis. *Cancer Cell* **41**, 1397–1406 (2023).
81. Gabitto, M. I. et al. Integrated multimodal cell atlas of Alzheimer's disease. Preprint at *Res. Sq*. https://doi.org/10.21203/rs.3.rs-2921860/v1 (2023).
82. Dong, X. et al. Accurate identification of single-nucleotide variants in whole-genome-amplified single cells. *Nat. Methods* **14**, 491–493 (2017).
83. Ren, P., Dong, X. & Vijg, J. Age-related somatic mutation burden in human tissues. *Front. Aging* **3**, 1018119 (2022).

84. Lawson, A. R. J. et al. Somatic mutation and selection at population scale. *Nature* **647**, 411–420 (2025).
85. Machado, H. E. et al. Diverse mutational landscapes in human lymphocytes. *Nature* **608**, 724–732 (2022).
86. Zhang, L. et al. Single-cell whole-genome sequencing reveals the functional landscape of somatic mutations in B lymphocytes across the human lifespan. *Proc. Natl Acad. Sci. USA* **116**, 9014–9019 (2019).
87. Ganz, J. et al. Contrasting somatic mutation patterns in aging human neurons and oligodendrocytes. *Cell* **187**, 1955–1970.e23 (2024).
88. Abascal, F. et al. Somatic mutation landscapes at single-molecule resolution. *Nature* **593**, 405–410 (2021).
89. Franco, I. et al. Whole genome DNA sequencing provides an atlas of somatic mutagenesis in healthy human cells and identifies a tumor-prone cell type. *Genome Biol.* **20**, 285 (2019).
90. Park, S. et al. Clonal dynamics in early human embryogenesis inferred from somatic mutation. *Nature* **597**, 393–397 (2021).
91. Heilbrun, E. E., Merav, M. & Adar, S. Exons and introns exhibit transcriptional strand asymmetry of dinucleotide distribution, damage formation and DNA repair. *NAR Genom. Bioinform.* **3**, lqab020 (2021).
92. Frigola, J. et al. Reduced mutation rate in exons due to differential mismatch repair. *Nat. Genet.* **49**, 1684–1692 (2017).
93. Doizuc, N. OceanOptics/pylr2: linear regression type II models. *GitHub* https://github.com/OceanOptics/pylr2 (2018).
94. de Magalhães, J. P., Costa, J. & Church, G. M. An analysis of the relationship between metabolism, developmental schedules, and longevity using phylogenetic independent contrasts. *J. Gerontol. A Biol. Sci. Med. Sci.* **62**, 149–160 (2007).
95. Davidson-Pilon, C. lifelines: survival analysis in Python. *J. Open Source Softw.* **4**, 1317 (2019).
96. Montine, T. J. et al. National Institute on Aging-Alzheimer's Association guidelines for the neuropathologic assessment of Alzheimer's disease: a practical approach. *Acta Neuropathol.* **123**, 1–11 (2012).
97. Nandi, S. P. et al. A universal duplex sequencing approach for accurate detection of somatic mutations. Preprint at *bioRxiv* https://doi.org/10.1101/2025.09.14.676103 (2025).
98. Cheng, Y. et al. Improved mutation detection in duplex sequencing data with sample-specific error profiles. Preprint at *bioRxiv* https://doi.org/10.1101/2025.07.13.664565 (2025).
99. Cook, R. D. Detection of influential observation in linear regression. *Technometrics* **19**, 15–18 (1977).
100. Cao, H. et al. Genome-wide profiles of DNA damage represent highly accurate predictors of mammalian age. *Aging Cell* **23**, e14122 (2024).
101. Kanehisa, M. & Goto, S. KEGG: Kyoto Encyclopedia of Genes and Genomes. *Nucleic Acids Res.* **28**, 27–30 (2000).
102. Ashburner, M. et al. Gene Ontology: tool for the unification of biology. The Gene Ontology consortium. *Nat. Genet.* **25**, 25–29 (2000).

Acknowledgements

This study was funded by the National Institutes of Health under awards U54 CA274502 and P41 GM103504. DNA sequencing was conducted at the IGM Genomics Center, University of California, San Diego. This publication includes data generated at the University of California, San Diego IGM Genomics Center utilizing an Illumina NovaSeq 6000 that was purchased with funding from a National Institutes of Health SIG grant (no. S10 OD026929). The Triton Shared Computing Cluster provided the computational resources used for DNA sequencing analyses. Figures were created, in part, in BioRender.

Author contributions

Z.K. designed the study, carried out the primary data analyses, and wrote the manuscript. A.B.D., D.H.M., B.S. and L.A. designed the study and wrote the manuscript. F.D. and P.P. designed the study and provided the mouse samples. K.L., S.S. and S.N. designed the study, performed the duplex sequencing experiment and wrote the manuscript. T.I. designed the study and wrote the manuscript.

Competing interests

T.I. is a co-founder, member of the advisory board and has an equity interest in Data4Cure and Serinus Biosciences. T.I. is a consultant for and has an equity interest in Ideaya Biosciences and Eikon Pharmaceuticals. The terms of these arrangements have been reviewed and approved by the University of California, San Diego in accordance with its conflict of interest policies. L.B.A. is a co-founder, CSO, scientific advisory member and consultant for Acurion (formerly io9), has equity and receives income. The terms of this arrangement have been reviewed and approved by the University of California, San Diego in accordance with its conflict of interest policies. L.B.A. is also a compensated member of the scientific advisory board of Inocras. The spouse of L.B.A. is an employee of Hologic. L.B.A. declares US provisional applications filed with UCSD with serial nos. 63/269033, 63/289601, 63/483237, 63/412835, 63/492348 and 63/366392 as well as a European patent application with application no. EP25305077.7. L.B.A. and S.P.N. also declare provisional patent application PCT/US2023/010679. L.B.A. is also an inventor of a US Patent 10,776,718 for source identification by non-negative matrix factorization. All other authors declare no competing interests.

Additional information

Extended data is available for this paper at https://doi.org/10.1038/s43587-026-01132-z.

Supplementary information The online version contains supplementary material available at https://doi.org/10.1038/s43587-026-01132-z.

Correspondence and requests for materials should be addressed to Trey Ideker.

Peer review information *Nature Aging* thanks Irene Franco, Yifen Yang, and the other, anonymous, reviewer(s) for their contribution to the peer review of this work. Peer reviewer reports are available.

https://doi.org/10.1038/s43587-026-01132-z

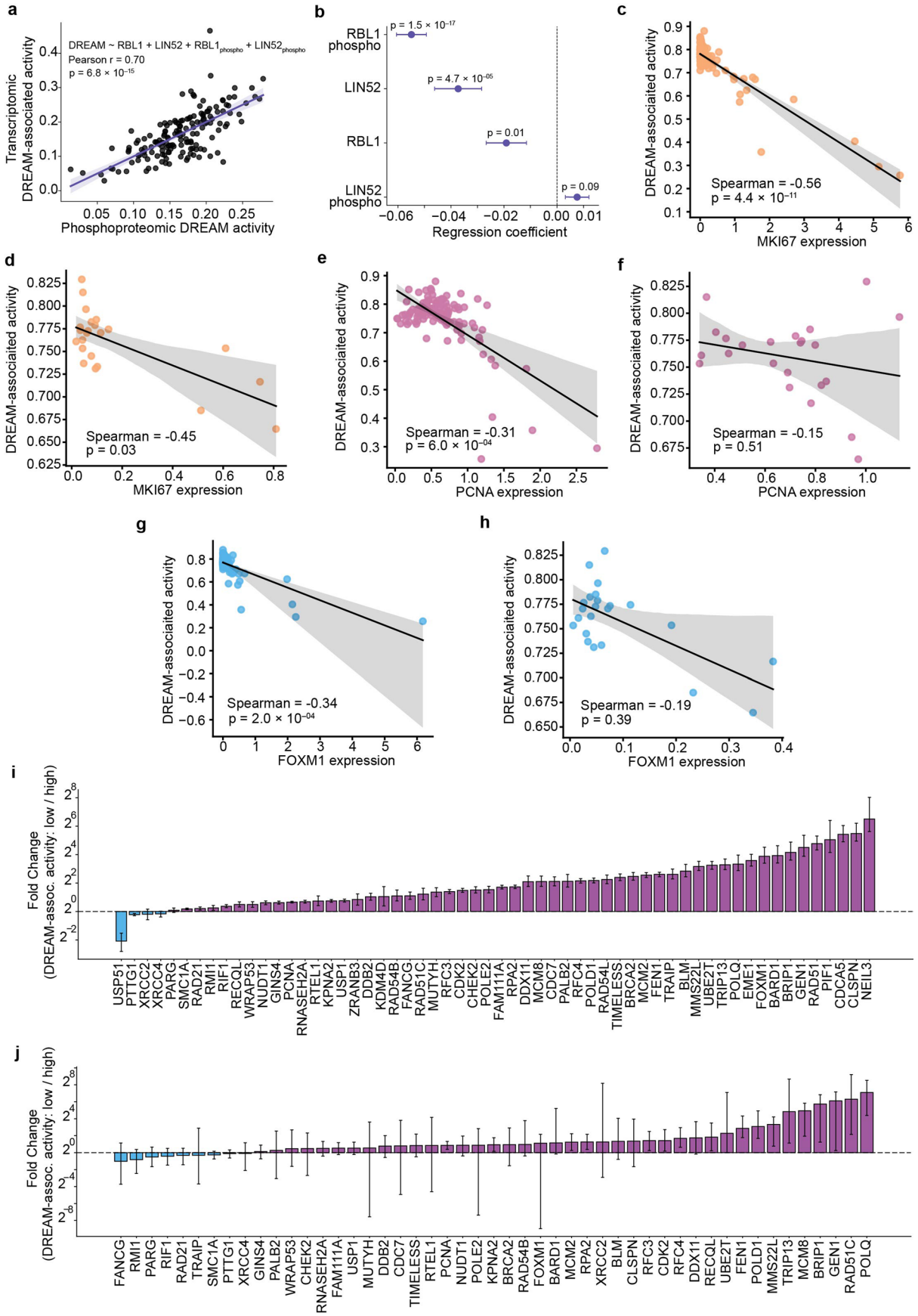

Extended Data Fig. 1 | See next page for caption.

https://doi.org/10.1038/s43587-026-01132-z

Extended Data Fig. 1 | DREAM target expression mirrors other activity measures. a) Scatter-plot of DREAM-associated activity in human tumor tissues inferred from either the protein abundance and phosphorylation status of DREAM complex components (x axis) or the gene expression of DREAM-target genes ("transcriptomic DREAM activity", y-axis, *n* = 160 individuals). Two-sided p value calculated based on the exact distribution of Pearson's r modeled as a beta function. **b**) Association of protein abundance and phosphorylation status of DREAM complex components (RBL1 and LIN52) with transcriptomic DREAM-associated activity in human tissues (*n* = 160 individuals). Dots and whiskers indicate the coefficient and standard error from a linear mixed effects model regressing DREAM-associated activity on the variables shown (**Methods**). Significance was calculated using two-sided t-tests. **c**) Scatter-plot of the mean expression of the proliferation marking gene *MKI67* versus the mean DREAM-associated activity, in each cell type (*n* = 120 cell types). Two-sided p value calculated modeling Spearman ρ's as a Student's t distribution. **d**) Similar to (**c**) but in each tissue type (*n* = 21 tissues). **e**) Similar to (**b**) but comparing DREAM-associated activity to *PCNA* expression. **f**) Similar to (**d**) but comparing DREAM-associated activity to *PCNA* expression. **g**) Similar to (**b**) but comparing DREAM-associated activity to *FOXM1* expression. **h**) Similar to (**d**) but comparing DREAM-associated activity to *FOXM1* expression. **i**) Log_2 fold change in expression of DREAM-regulated DNA repair genes (*n* = 67 genes) comparing cells in the lowest versus highest DREAM-associated activity quintiles (*n* = 4 eighteen-month-old mice, *n* = 34,027 cells). Error bars represent 95% bootstrap confidence intervals (*n* = 1,000 iterations). Purple and blue bars indicate higher and lower expression in low DREAM cells, respectively. **j**) Similar to (**i**) but only in liver cells (*n* = 49 expressed genes, *n* = 1,180 liver cells, *n* = 4 mice).

https://doi.org/10.1038/s43587-026-01132-z

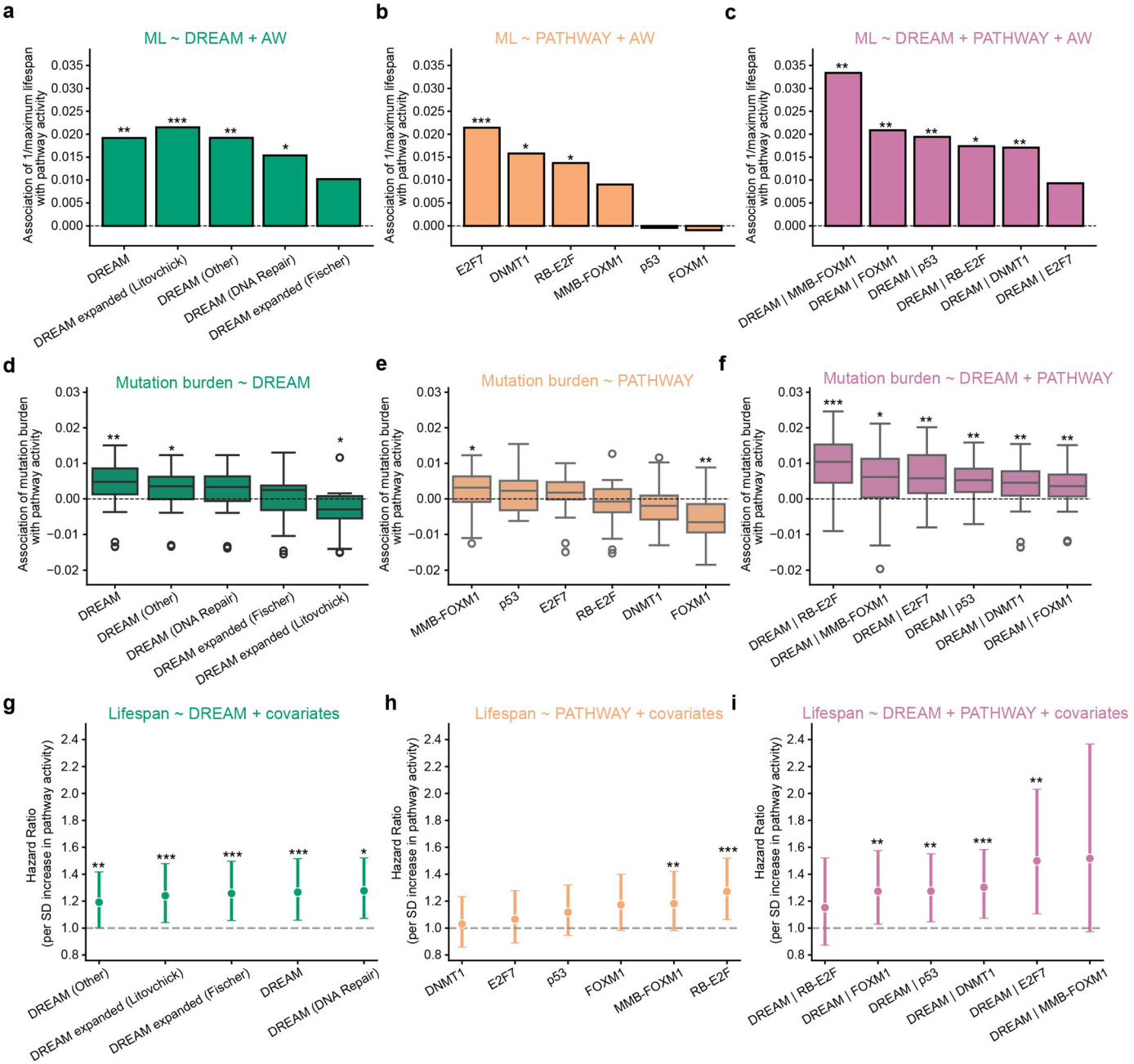

Extended Data Fig. 2 | See next page for caption.

https://doi.org/10.1038/s43587-026-01132-z

Extended Data Fig. 2 | DREAM-associated activity in single cells. a) Barplots showing standardized regression coefficients associating the inverse of maximum lifespan (ML) with DREAM-related pathway activities in the liver across species (n = 92 species, n = 241 liver samples). Each bar represents the coefficient from an OLS regression model fit on species-level means (1/maximum lifespan ~ pathway activity + $\log_2$-adult-weight). Pathways include the core DREAM signature and related sub-signatures: DREAM (DNA Repair), DREAM (Other), DREAM expanded (Fischer), and DREAM expanded (Litovchick) (**Methods**). (***), (**), and (*) indicate $p < 0.001$, $p < 0.01$, and $p < 0.05$, respectively, from two-sided t-tests on regression coefficients. **b**) Similar to (**a**), but for other cell-cycle or chromatin remodeling related pathways tested in individual regression models for an association with 1/maximum lifespan (1/maximum lifespan ~ pathway activity + $\log_2$-adult-weight). Pathways include MMB-FOXM1, p53, RB-E2F, DNMT1, E2F7, and FOXM1. **c**) Similar to (**a**), but showing the standardized DREAM coefficient when controlling for each of the pathways in (**b**). Each bar represents the DREAM coefficient from a multiple regression model (1/maximum lifespan ~ DREAM-associated activity + pathway activity + $\log_2$-adult-weight). The x axis labels indicate which pathway was included as a covariate alongside DREAM (for example, "DREAM | MMB-FOXM1"). **d**) Box plots showing the distribution of standardized regression coefficients associating DREAM-related pathway activities with somatic mutation burden in single cells (n = 34,027 cells) from 18-month-old mice (n = 4 mice). Each box represents the distribution of coefficients from OLS regression models (mutation burden ~ pathway activity) run separately within each tissue (n = 21 tissue types). Pathways include the core DREAM signature and related sub-signatures (**Methods**). (***), (**), and (*) indicate pathways with distribution of coefficients significantly different from zero (Wilcoxon signed-rank test; $p < 0.001$, $p < 0.01$, $p < 0.05$, respectively). **e**) Similar to (**d**), but for other cell-cycle or chromatin remodeling related pathways tested in individual regression models for an association with mutation burden in each tissue (mutation burden ~ pathway activity). **f**) Similar to (**d**), but showing the standardized DREAM coefficient after adjustment for each alternate pathway. Each box represents coefficients from multiple regression models (mutation burden ~ DREAM + pathway) run separately within each tissue. **g**) Point plot showing hazard ratios from Cox proportional hazard models associating DREAM-related pathway activities with mouse survival on a high-fat diet (HFD) (n = 612 mice, Methods). Points indicate hazard ratios and whiskers denote 95% confidence intervals. Models include interaction terms for diet and control for principal components of mouse metabolic phenotypes, sequencing depth, and weight change (**Methods**). (***), (**), and (*) indicate $p < 0.001$, $p < 0.01$, and $p < 0.05$, respectively, from two-sided Wald tests. **h**) Similar to (**g**), but for other cell-cycle or chromatin remodeling related pathways tested in individual Cox models for an association with survival. **i**) Similar to (**g**), but showing the hazard ratio for DREAM-associated activity after adjustment for each alternate pathway in (**h**). Each point represents the DREAM hazard ratio from a Cox model including both DREAM and the indicated pathway as predictors. The x-axis labels indicate which pathway was included as a covariate alongside DREAM.

https://doi.org/10.1038/s43587-026-01132-z

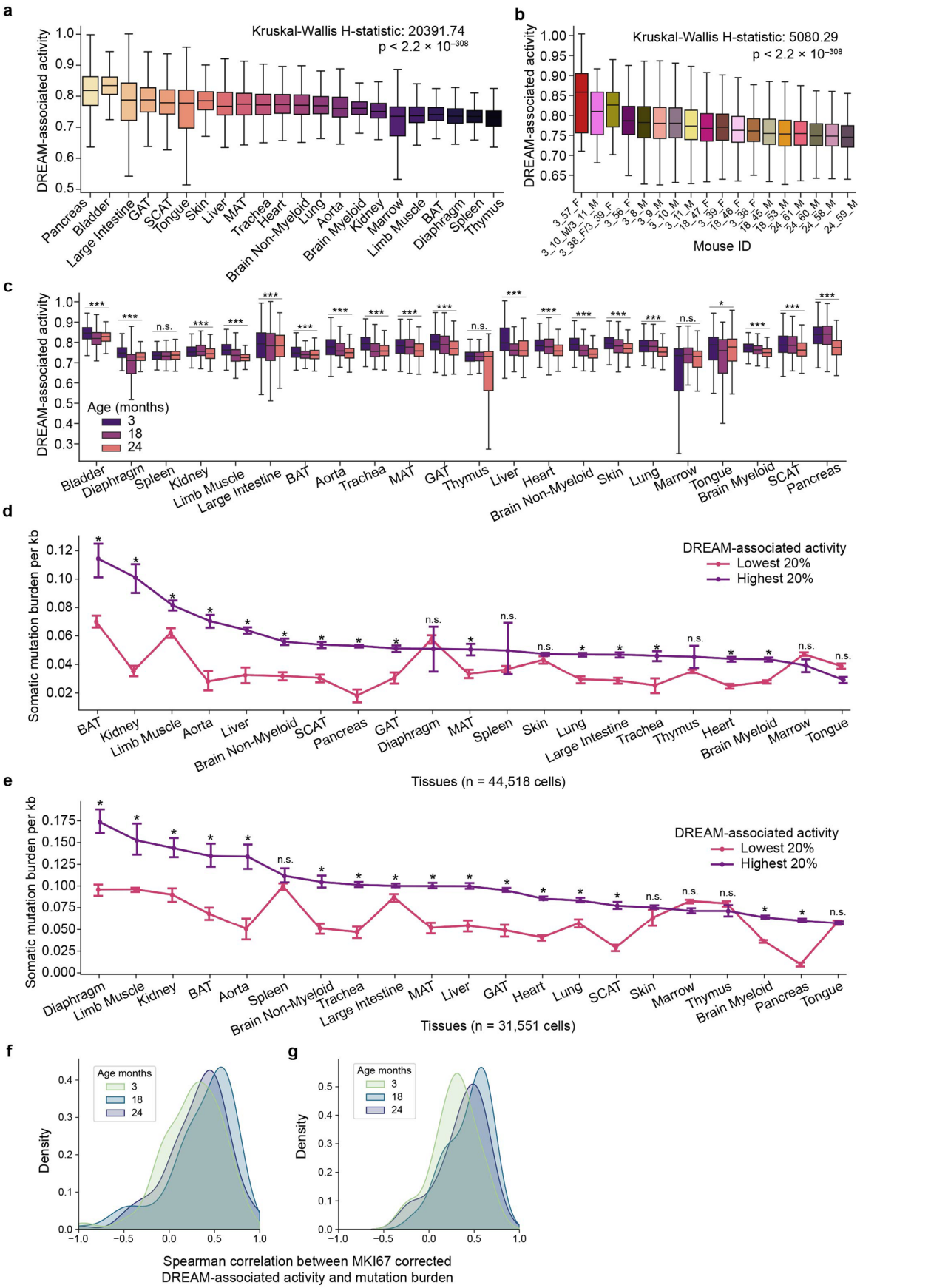

Extended Data Fig. 3 | See next page for caption.

https://doi.org/10.1038/s43587-026-01132-z

Extended Data Fig. 3 | Mutation rate across species. a) Box plots of the distribution of DREAM complex activity by tissue across all cells from all mice (n = 110,824 cells, n = 18 mice). Two-sided p value from a Kruskal-Wallis test for a difference of distribution between tissues is shown. Boxes show interquartile range (IQR) with median line; whiskers extend to 1.5 IQR **b**) Box plots of the distribution of DREAM complex activity by mouse across all cells from all mice (n = 110,824 cells, n = 18 mice). Two-sided p value from a Kruskal-Wallis test for a difference of distribution between tissues is shown. **c**) Box plots of the distribution of DREAM-associated activity scores in each tissue at each age (n = 110,824 cells, n = 18 mice). (***), (*), and (n.s.) indicate p values calculated by modeling Spearman ρ's as a Student's t distribution of $p < 1.0 \times 10^{-7}$, $p < 0.01$, and $p \geq 0.01$, respectively. **d**) The somatic mutation burden per kilobase in cells (n = 44,518 cells, n = 10 mice) stratified by DREAM complex activity in 3 month old mice. Cells were partitioned into those with the highest and lowest 20% of DREAM complex activities within each tissue. Error bars denote 95% confidence intervals. (*) indicates $p < 0.0023$ (Bonferroni-corrected p-value) and (n.s.) indicates $p \geq 0.0023$, based on a two-sided Mann–Whitney test. **e**) Similar to (**c**), but for cells from 24 month old mice (n = 31,551 cells, n = 4 mice). **f**) The distribution of Spearman correlation coefficients between MKI67-corrected DREAM complex activity and somatic mutation burden, within each cell type and age (n = 120 cell types, n = 110,824 cells, **Methods**). **g**) Similar to (**e**) but within each tissue type (n = 21 tissues, n = 110,824 cells).

https://doi.org/10.1038/s43587-026-01132-z

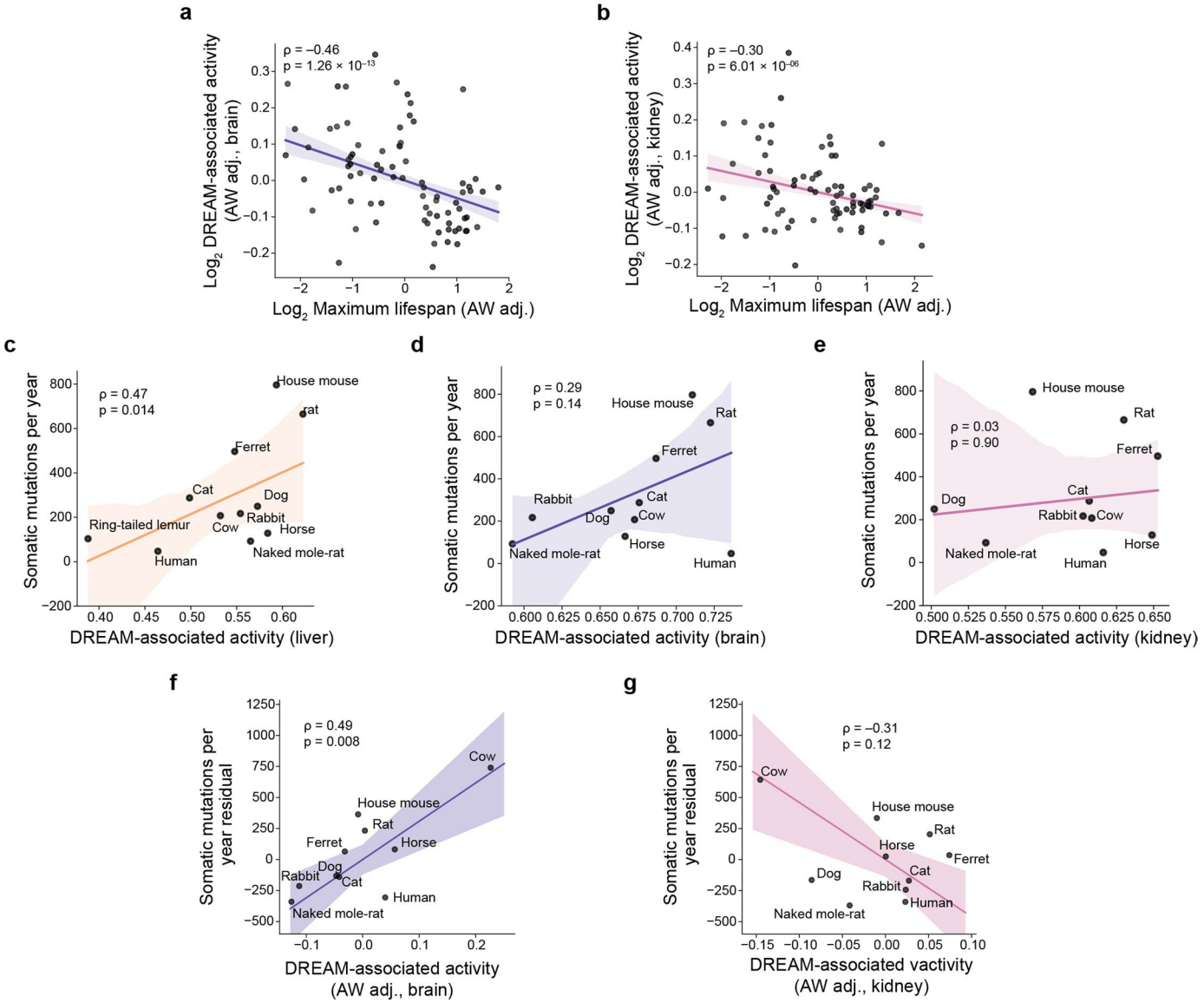

Extended Data Fig. 4 | Connection of DREAM-associated activity with DNA damage. a) Scatter-plot and reduced major axis regression depicting the average adult weight (AW) adjusted DREAM-associated activity and lifespan across species ($n = 92$ species, **Methods**). Both axes are shown on a logarithmic scale. **b**) Similar to (**a**), but DREAM-associated activity is measured in the kidney. **c**) Scatter-plot and reduced major axis regression of the mean DREAM-associated activity in the liver of a species and somatic mutation rate in the colon in that same species ($n = 11$ species, **Methods**). **d**) Similar to (**c**), but DREAM-associated activity is measured in the brain. **e**) Similar to (**c**), but DREAM-associated activity is measured in the kidney. **f**) Scatter-plot and reduced major axis regression depicting the average AW adjusted DREAM-associated activity and somatic mutation rate (in the brain and colon, respectively) across species ($n = 11$ species, **Methods**). **g**) Similar to (**f**), but DREAM-associated activity measured in the kidney.

https://doi.org/10.1038/s43587-026-01132-z

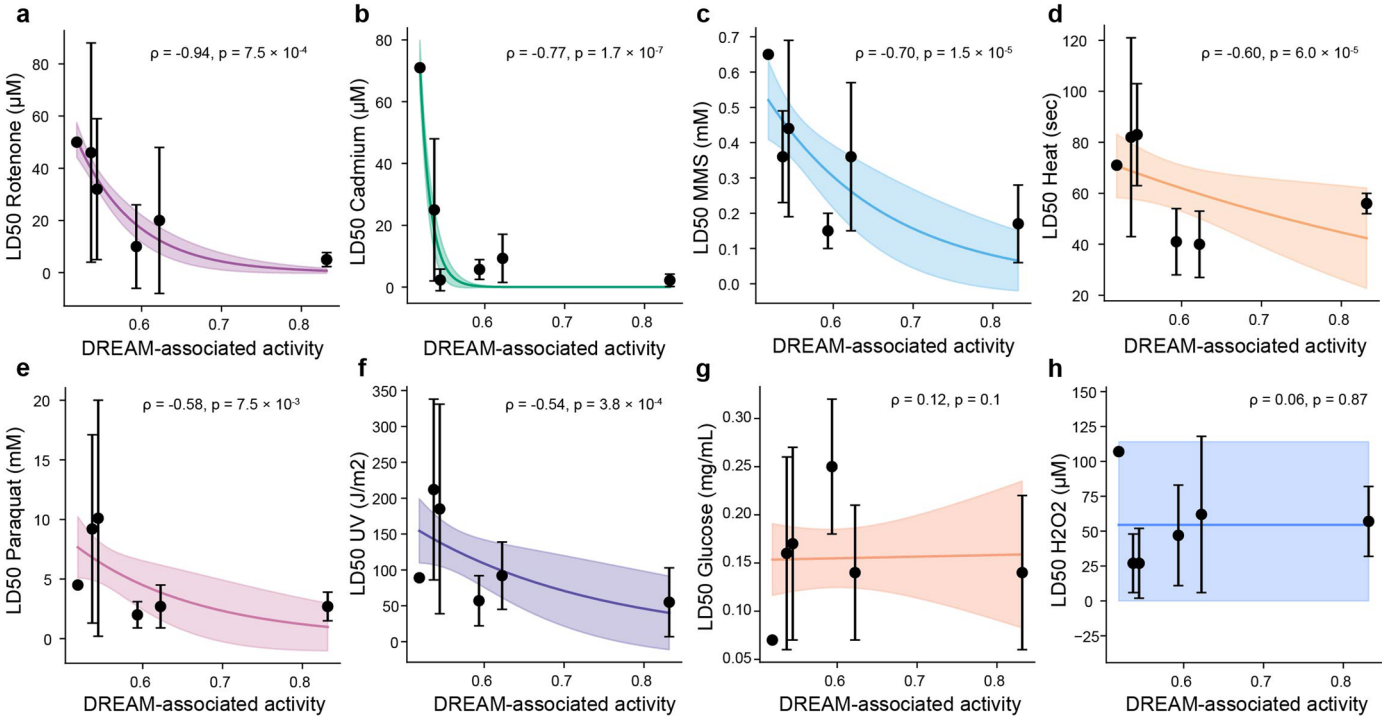

Extended Data Fig. 5 | Survival and DREAM-associated activity in mice. **a-h**) Scatter plots of species-specific liver DREAM complex activity vs. resistance (LD50) of fibroblasts from six species to damaging agents (from Harper et al.[2]). The points and error bars indicate the mean and 95% confidence interval of the LD50 of all cell lines of a species. The colored line and shaded area indicate the fit of an exponential decay model and 95% confidence interval, respectively. From left to right in each plot species include: the north american beaver ($n = 1$ cell line), red squirrel ($n = 9$ cell lines), white-footed mouse ($n = 7$ cell lines), house mouse ($n = 9$ cell lines), Norway rat ($n = 6$ cell lines), and deer mouse ($n = 5$ cell lines). Significance was calculated using a two-sided t-test between the cell lines of the 3 species with highest and lowest DREAM-associated activity, respectively.

https://doi.org/10.1038/s43587-026-01132-z

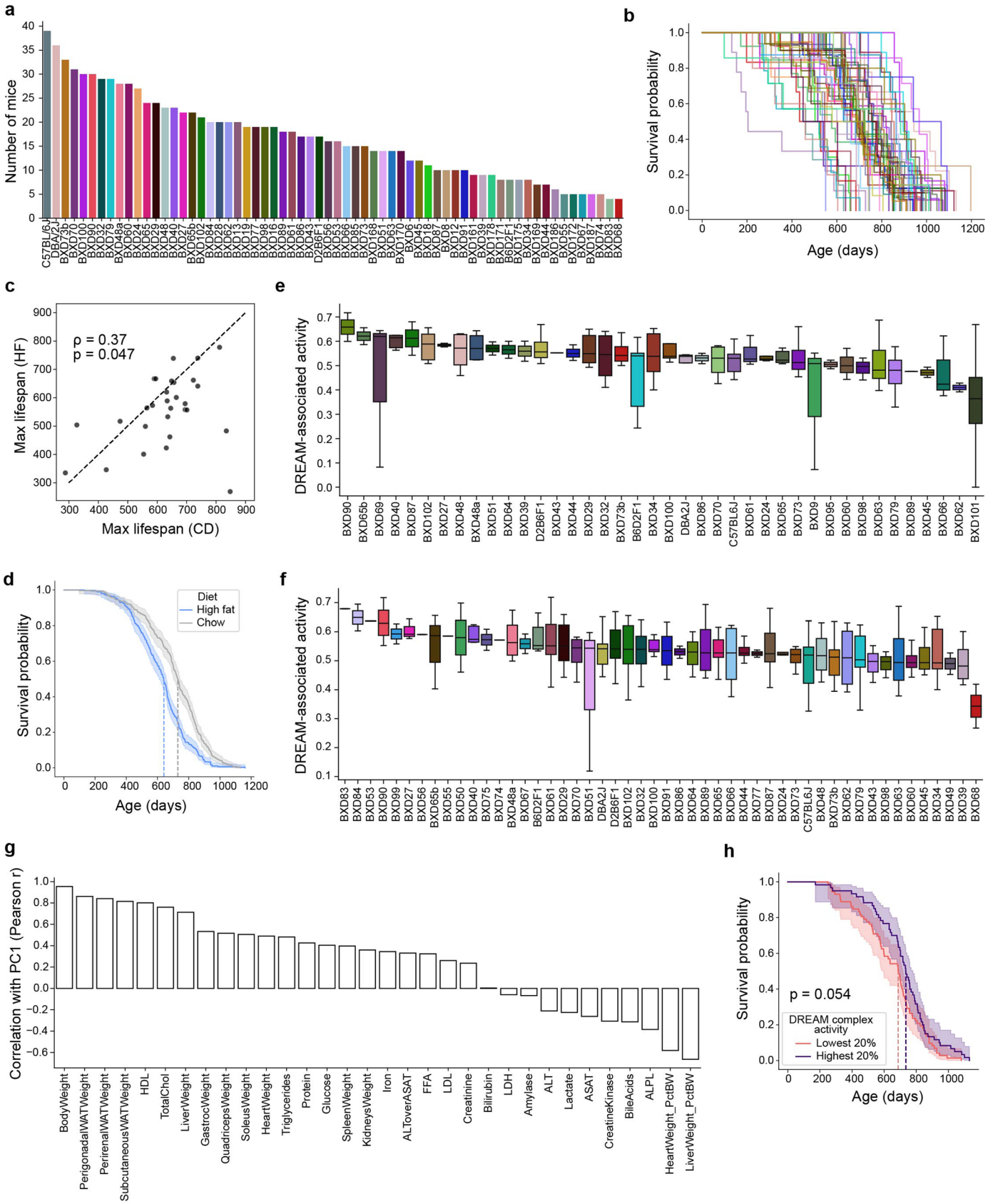

Extended Data Fig. 6 | See next page for caption.

https://doi.org/10.1038/s43587-026-01132-z

Extended Data Fig. 6 | Somatic mutations in human tissues. a) Bar chart of the number of mice of each strain (n = 50 strains, n = 882 mice). **b**) Kaplan–Meier survival curve for each strain in (**a**). **c**) Scatter-plot comparing the maximum lifespan of each strain on the chow diet (CD, x axis) to the high-fat diet (HFD, y-axis, n = 29 strains profiled for lifespan and RNA-seq on both diets). **d**) Kaplan–Meier survival curve for mice of all strains on the CD (n = 498 mice) compared to the HFD (n = 522 mice). The dark line and shaded area indicate the proportion of mice surviving to a particular age and the 95% confidence interval of this survival estimate, respectively. Dashed lines indicate the median survival of each group. **e**) Box plots of the distribution of DREAM complex activity in mice of each strain fed the HFD (n = 120 mice profiled for liver gene expression). **f**) Similar to (**e**) but for mice fed the CD (n = 150 mice profiled for liver gene expression). **g**) Correlation of the standardized values of each covariate with principal component 1 (that is, "PC1 loading", n = 270 mice, **Methods**). **h**) Kaplan–Meier survival curve of CD fed mice belonging to strains with the highest vs lowest 20% of DREAM complex activities (purple vs. pink, n = 132 mice, n = 15 strains). The dark line and shaded area indicates the proportion of mice surviving to a particular age and the 95% confidence interval of this survival estimate, respectively. Dashed lines indicate the median survival of each group. P value calculated from a two-sided log-rank test.

https://doi.org/10.1038/s43587-026-01132-z

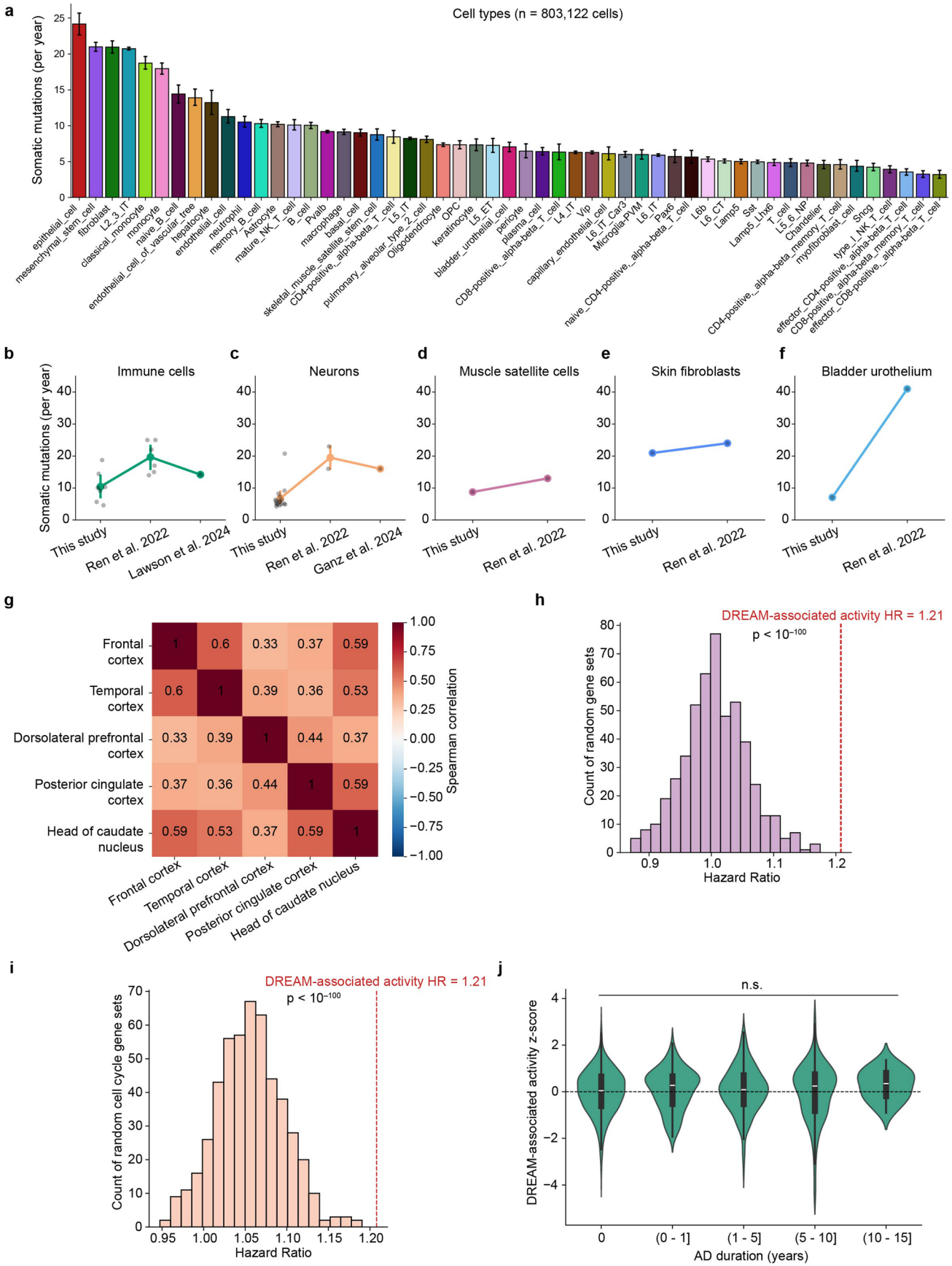

Extended Data Fig. 7 | See next page for caption.

https://doi.org/10.1038/s43587-026-01132-z

Extended Data Fig. 7 | Duplex sequencing. a) Barplot indicating the mean and 95% confidence interval of the number of somatic mutations identified in each cell per year (normalized to haploid genome size, **Methods**) grouped by cell type (n = 803,122 cells, n = 90 individuals). **b-f**) Line plots comparing the number of somatic mutations per year identified by "this study" compared with previous estimates using DNA sequencing. Dark points indicate the mean mutation rate for a single cell type in a particular study, while the colored points indicate the mean and 95% confidence interval of these mutation rates. The x axis lists the study from which the respective data came. **g**) Heatmap depicting the pairwise Spearman correlations of DREAM complex activity in different brain regions of the same individual (n = 1,101 individuals, 2,776 samples, mean 2.4 ± std 1.0 brain regions per individual). All pairwise correlations are significant ($p < 0.0004$). **h**) Histogram showing the distribution of hazard ratios from Cox proportional hazards models predicting age at AD diagnosis (using the same covariates as Fig. 6g, n = 1,101 individuals, **Methods**) using the ssGSEA enrichment of 500 randomly chosen sets of genes. HR of DREAM-regulated gene expression is shown for reference (red, dashed, vertical line). P value shown for two-sided one sample t-test. **i**) Similar to (**h**), but selecting gene sets randomly from all cell-cycle genes annotated by KEGG[101] or Gene Ontology[102] (n = 1,801 cell cycle genes). **j**) Violin plots showing the distribution of DREAM-associated activity values in individual samples (n = 1,101 individuals), Z-score normalized within each brain tissue, stratified by the duration each individual had AD before death. No pairwise comparisons between AD duration groups (violin plots) were significant ($p < 0.05$) based on two-sided Mann–Whitney U tests.

https://doi.org/10.1038/s43587-026-01132-z

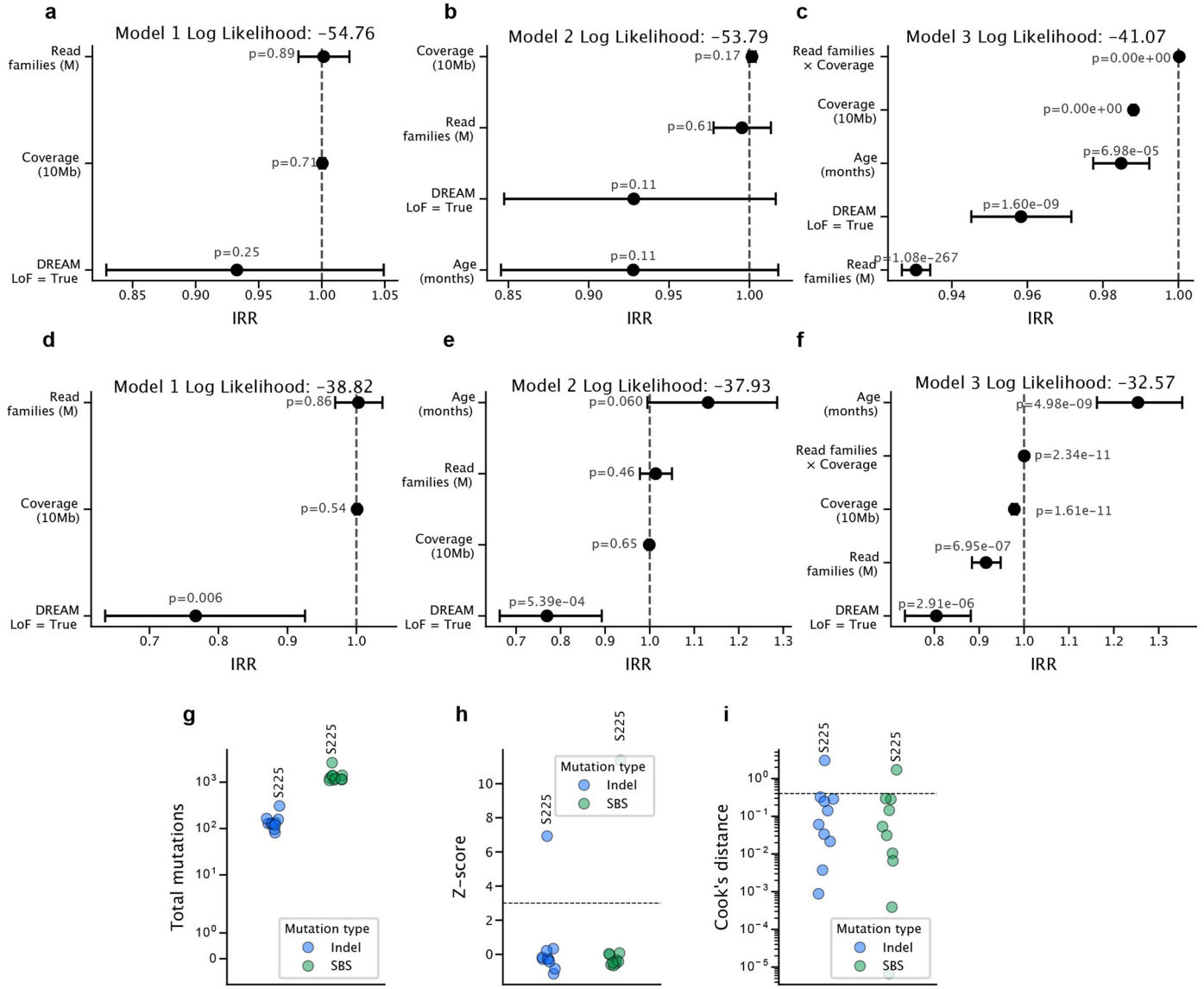

Extended Data Fig. 8 | The association of DREAM-related pathways with lifespan and somatic mutation burden. a-c) Associations between covariates and single-base substitution (SBS) mutations per cell from negative binomial regression (Methods). Points and whiskers show incidence rate ratios (IRR) with 95% CIs. Model 1 (**e**) includes DREAM K.O. status, read families (per million) and coverage (per 10 Mb). Model 2 (**f**) adds age (months). Model 3 (**g**) further includes a read families × coverage interaction. P values are from two-sided Wald tests. Less-negative log-likelihood indicates better fit. **d-f**) Similar to (**a-c**), but for insertion/deletion (ID) mutations. **g–i**) Per-mouse mutation burden and outlier diagnostics by mutation type. Each point is one mouse; colors denote mutation class, with outlier sample S225 labeled. (**g**) Total mutations per mouse ($\log_{10}$ scale). (**h**) Z-scores used to assess outlier status – the dashed line marks the Z-score threshold of 3. (i) Cook's distance from the regression model ($\log_{10}$ scale) – the dashed line marks the Cook's distance threshold of 1. Samples above the thresholds on all mutation classes are considered outliers.

nature portfolio

Corresponding author(s): Trey Ideker

Last updated by author(s): Mar 14, 2026

Reporting Summary

Nature Portfolio wishes to improve the reproducibility of the work that we publish. This form provides structure for consistency and transparency in reporting. For further information on Nature Portfolio policies, see our Editorial Policies and the Editorial Policy Checklist.

Statistics

For all statistical analyses, confirm that the following items are present in the figure legend, table legend, main text, or Methods section.

n/a	Confirmed
☐	☒ The exact sample size (*n*) for each experimental group/condition, given as a discrete number and unit of measurement
☐	☒ A statement on whether measurements were taken from distinct samples or whether the same sample was measured repeatedly
☐	☒ The statistical test(s) used AND whether they are one- or two-sided *Only common tests should be described solely by name; describe more complex techniques in the Methods section.*
☐	☒ A description of all covariates tested
☐	☒ A description of any assumptions or corrections, such as tests of normality and adjustment for multiple comparisons
☐	☒ A full description of the statistical parameters including central tendency (e.g. means) or other basic estimates (e.g. regression coefficient) AND variation (e.g. standard deviation) or associated estimates of uncertainty (e.g. confidence intervals)
☐	☒ For null hypothesis testing, the test statistic (e.g. *F*, *t*, *r*) with confidence intervals, effect sizes, degrees of freedom and *P* value noted *Give P values as exact values whenever suitable.*
☒	☐ For Bayesian analysis, information on the choice of priors and Markov chain Monte Carlo settings
☒	☐ For hierarchical and complex designs, identification of the appropriate level for tests and full reporting of outcomes
☐	☒ Estimates of effect sizes (e.g. Cohen's *d*, Pearson's *r*), indicating how they were calculated

Our web collection on statistics for biologists contains articles on many of the points above.

Software and code

Policy information about availability of computer code

Data collection	All custom algorithms and analysis code are available in the GitHub repository at https://github.com/zanekoch/dream_proj.
Data analysis	All analyses were performed in Python 3.10. Data analysis was conducted using Pandas 1.5.3, SciPy 1.10.0, Pingouin 0.5.3, and Statsmodels 0.13.5. Data were visualized with Seaborn 0.12.1 and Matplotlib 3.7.1. No statistical method was used to predetermine sample size, the experiments were not randomized, and the investigators were not blinded to allocation during experiments and outcome assessment. Specific statistical approaches used are noted in the respective methods sections and figure captions.

For manuscripts utilizing custom algorithms or software that are central to the research but not yet described in published literature, software must be made available to editors and reviewers. We strongly encourage code deposition in a community repository (e.g. GitHub). See the Nature Portfolio guidelines for submitting code & software for further information.

Data

Policy information about availability of data

All manuscripts must include a data availability statement. This statement should provide the following information, where applicable:

- Accession codes, unique identifiers, or web links for publicly available datasets
- A description of any restrictions on data availability
- For clinical datasets or third party data, please ensure that the statement adheres to our policy

Raw UD-sequencing data can be accessed on the Sequence Read Archive (SRA) under BioProject accession PRJNA1436559. Other data can be accessed through the respective publications (see Supplementary Table 1).

Research involving human participants, their data, or biological material

Policy information about studies with human participants or human data. See also policy information about sex, gender (identity/presentation), and sexual orientation and race, ethnicity and racism.

Reporting on sex and gender	The study uses data from publicly available datasets. For the mouse studies (Tabula Muris Senis), both male and female mice were included as provided by the original consortium. For the human Alzheimer's disease analyses (SEA-AD and ROSMAP), sex was included as a covariate in the Cox proportional hazard model predicting age at AD diagnosis. Sex was determined as reported in the original datasets. Sex- and gender-based analyses were not separately performed, as the primary biological variables of interest (DREAM-associated activity, somatic mutation burden) operate at the cellular and molecular level. The study was not designed to test sex-specific hypotheses.
Reporting on race, ethnicity, or other socially relevant groupings	N/A. The study does not use race, ethnicity, or other socially constructed categorization variables.
Population characteristics	Human participants include 90 individuals (80 with AD/neurodegeneration, 10 cognitively normal) from the Tabula Sapiens and SEA-AD consortia, aged 33–102 years (mean 85.2 ± 13.5). The ROSMAP cohort includes 1,101 deceased donors with post-mortem brain tissue from multiple brain regions. Covariates in the Cox model included DREAM-associated activity, number of APOE ε4 alleles, sex, RNA sequencing depth, gene detection count, and post-mortem interval.
Recruitment	N/A. All data were derived from previously published, publicly available datasets.
Ethics oversight	Animal protocols for the DREAM loss-of-function mouse experiment were approved as described in the original publication (Perampalam et al. 2021). All other data were obtained from publicly available repositories with ethics approvals described in their respective source publications.

Note that full information on the approval of the study protocol must also be provided in the manuscript.

Field-specific reporting

Please select the one below that is the best fit for your research. If you are not sure, read the appropriate sections before making your selection.

☒ Life sciences ☐ Behavioural & social sciences ☐ Ecological, evolutionary & environmental sciences

For a reference copy of the document with all sections, see nature.com/documents/nr-reporting-summary-flat.pdf

Life sciences study design

All studies must disclose on these points even when the disclosure is negative.

Sample size	The maximum sample size constrained by available data and/or samples was used.
Data exclusions	Outliers were excluded based on various measures described in the manuscript.
Replication	ey findings were replicated across independent datasets and biological systems. The association between DREAM-associated activity and somatic mutation burden was observed independently in mouse single cells (Tabula Muris Senis, n = 110,824 cells) and human single cells (Tabula Sapiens and SEA-AD, n = 803,122 cells). The association between DREAM-associated activity and lifespan was consistent across 92 mammalian species and across three tissue types (liver, brain, kidney). The link to Alzheimer's disease was replicated across two independent human cohorts (SEA-AD, n = 83 individuals; ROSMAP, n = 1,101 individuals). The causal role of DREAM in mutation accumulation was supported by the DREAM loss-of-function mouse experiment with biological replicates (n = 4 LoF, n = 5 controls). All attempts at replication were successful.
Randomization	Randomization was not applicable to the observational components of this study, which analyzed existing publicly available datasets.
Blinding	Blinding was not applicable to the computational analyses, which used quantitative, algorithmic pipelines applied uniformly to all samples.

Reporting for specific materials, systems and methods

We require information from authors about some types of materials, experimental systems and methods used in many studies. Here, indicate whether each material, system or method listed is relevant to your study. If you are not sure if a list item applies to your research, read the appropriate section before selecting a response.

Materials & experimental systems

n/a	Involved in the study
☒	☐ Antibodies
☒	☐ Eukaryotic cell lines
☒	☐ Palaeontology and archaeology
☐	☒ Animals and other organisms
☒	☐ Clinical data
☒	☐ Dual use research of concern
☒	☐ Plants

Methods

n/a	Involved in the study
☒	☐ ChIP-seq
☒	☐ Flow cytometry
☒	☐ MRI-based neuroimaging

Animals and other research organisms

Policy information about studies involving animals; ARRIVE guidelines recommended for reporting animal research, and Sex and Gender in Research

Laboratory animals	DREAM loss-of-function mice (p107^D/D^ p130^−/−^, n = 4) and littermate controls (p107^D/D^ p130^fl/fl^, n = 5), which received tamoxifen at 8 weeks of age and were followed to natural death, as described in Perampalam et al. 2021.
Wild animals	N/A
Reporting on sex	N/A
Field-collected samples	N/A
Ethics oversight	Animal protocols for the DREAM loss-of-function mouse experiment were approved as described in Perampalam et al. 2021.

Note that full information on the approval of the study protocol must also be provided in the manuscript.

Plants

Seed stocks	n/a
Novel plant genotypes	n/a
Authentication	n/a